DOI: 10.1002/chem.200600724

VIP

Tuning the Electronic Communication in Heterobimetallic Mixed-Valence Ions of (1-Ferrocenyl)- and (2-Ferrocenyl)indenyl Rhodium Isomers

Saverio Santi,*[a] Laura Orian,[a] Christian Durante,[a] Annalisa Bisello,[a] Franco Benetollo,[b] Laura Crociani,[b] Paolo Ganis,[a] and Alberto Ceccon*[a]

Abstract: A series of heterobimetallic complexes of general structure [RhL_2-{η^5-(2-ferrocenyl)indenyl}] (L_2 = cod, nbd, L = CO; cod = cyclooctadiene; nbd = norbornadiene) has been synthesised with the aim of tuning the metal–metal interaction in their mixed-valence ions generated both by chemical and electrochemical oxidation, and the results are compared with those obtained for [RhL_2{η^5-(1-ferrocenyl)indenyl}] isomers. Crystallographic studies and DFT calculations provide a detailed description of the structural and electronic features of these complexes evidencing a significant difference in the extent of planarity of the flexible bridging ligand between the 1- and 2-ferrocenyl isomers. Independent experimental probes, in particular the potential splitting in the cyclic voltammograms and the IT bands in the near-IR spectra, are rationalised in the framework of Marcus–Hush theory and at quantum chemistry level by DFT and TD-DFT methods. These methods allow us to establish a trend based on the magnitude of iron–rhodium electronic coupling H_{ab} ranging from valence trapped to almost delocalised ions. The quasi planar bridge and the olefin ancillary ligands make [Rh(nbd)-{η^5-(2-ferrocenyl)indenyl}]$^+$ and [Rh-(cod){η^5-(2-ferrocenyl)indenyl}]$^+$ rare examples of heterobimetallic systems which can be classified as borderline Class II/Class III species.

Keywords: electron transfer · ferrocene · heterobimetallic compounds · mixed-valent compounds · rhodium

Introduction

Understanding and control of intramolecular electron-transfer reactions represent two of the major issues of the current organometallic research.[1–3] In the case of bimetallic complexes in which two metals are connected by an unsaturated organic bridge, it has long been known that the magnitude of the electronic coupling is largely dependent on the structure and stereochemistry of the bridging ligand,[2m,4] and increases if the spacer is forced to adopt a planar geometry.[2j] In this regard, we have recently shown[5] that the electronic coupling between iron and chromium in the mixed-valence ions of the two isomers [$Cr(CO)_3${η^5-(2-ferrocenyl)indene}] and [$Cr(CO)_3${η^5-(3-ferrocenyl)indene}] is more pronounced in the former due to the almost coplanarity (torsion angle value 10°) of the indenyl and cyclopentadienyl (Cp) moieties in the bridging ligand. In contrast, such planarity is lost in the 3-ferrocenyl isomer compound where the torsion angle is 31°.

For the activation of a metal induced by an adjacent oxidised ferrocenyl group in heterobimetallic complexes, another example is represented by iron–rhodium systems. There is enormous interest in the chemical reactivity of rhodium complexes, especially in terms of their suitability for catalytic systems in which the generation of a vacancy at the metal represents the first and more important step of the catalytic cycle.[6,8] In the heteronuclear complexes of iron and rhodium [Rh(L){CpFe-(μ-η^5:η^5-*as*-indacenediide}] (L = cod, nbd; cod = cyclooctadiene; nbd = norbornadiene), the distance between the metals and their reciprocal *syn* or *anti* configu-

[a] Prof. S. Santi, Dr. L. Orian, Dr. C. Durante, Dr. A. Bisello, Prof. P. Ganis, Prof. A. Ceccon
Dipartimento di Scienze Chimiche
Università degli Studi di Padova, via Marzolo 1
35131 Padova (Italy)
Fax: (+39) 049-827-5239
E-mail: saverio.santi@unipd.it
alberto.ceccon@unipd.it

[b] Dr. F. Benetollo, Dr. L. Crociani
CNR, Istituto di Chimica Inorganica e delle Superfici
Corso Stati Uniti 4, 35127 Padova (Italy)

Supporting information for this article is available on the WWW under http://www.chemeurj.org/ or from the author. It contains electrochemical details and CVs of **1**-cod, **1**-nbd, **1**-CO; UV-Vis spectra of **1**-cod$^{0/+}$, **1**-nbd$^{0/+}$, **1**-CO$^{0/+}$, **2**-cod$^{0/+}$, **2**-nbd$^{0/+}$, **2**-CO$^{0/+}$; B3LYP/LANL2DZ,6-31+G* optimised geometries, most important TD-DFT vertical excitation energies and oscillator strengths of **1**-nbd$^{0/+}$, **1**-CO$^{0/+}$, **2**-cod$^{0/+}$, **2**-CO$^{0/+}$, pictures of the HOMOs of the neutral complexes at ZORA/TZ2P level of theory.

ration with respect to the bridging plane are certain and imposed by the rigidity and planarity of indacenyl ligands.[9] The results indicate the existence of a strong metal–metal electronic coupling in the radical cation of the *anti* isomers. In contrast, the oxidation of the *syn* isomer showed that the two metal units behave as two non-interacting centres, because of the bending of the bridging ligand induced by the steric hindrance between the unsubstituted Cp group and the ancillary cod ligand of rhodium.

The results on both iron–chromium and iron–rhodium complexes prompted us to investigate the phenomenon of electronic communication between the metals in the isomers of general formula [$RhL_2\{\eta^5$-(1-ferrocenyl)indenyl}] (**1**) and [$RhL_2\{\eta^5$-(2-ferrocenyl)indenyl}] (**2**) (L_2 = cod, nbd, L = CO) (Scheme 1), in which the fulvalenyl-like bridge has a high degree of torsional freedom which is different in the two isomers.

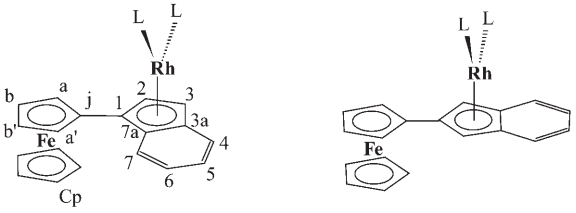

L_2 = cod (**1**-cod, **2**-cod)
L_2 = nbd (**1**-nbd, **2**-nbd)
L = CO (**1**-CO, **2**-CO)

Scheme 1.

We report here the synthesis of [Rh(cod)$\{\eta^5$-(2-ferrocenyl)indenyl}] (**2**-cod), [Rh(nbd)η^5-(2-ferrocenyl)indenyl}] (**2**-nbd) and [$Rh(CO)_2\{\eta^5$-(2-ferrocenyl)indenyl}] (**2**-CO), the X-ray structures of **2**-cod and **2**-CO together with that of (2-ferrocenyl)indene. Cyclic voltammetry (CV) of **2**-cod and **2**-CO was carried out in THF and CH_2Cl_2 with different supporting electrolytes, nBu_4NBF_4, nBu_4NPF_6, and $nBu_4NB(C_6F_5)_4$. The IR and near-IR spectra of the corresponding mixed-valence ions, obtained by variable temperature spectroelectrochemistry in different media, were recorded. In the near-IR region intervalence electron transfer occurs in mixed-valence compounds in which two or more redox sites exist in different oxidation states.[3m,n] The data will be compared with those obtained for **1**-cod, **1**-nbd and **1**-CO in order to verify how 1) the modification of the torsion angle between the indenyl and Cp moieties, 2) the type of ancillary ligand, and 3) the nature of the medium, may tune the extent of the electronic communication between the two metals.

Density functional theory (DFT) calculations,[10] carried out both on neutral and charged species, quantify and rationalise the geometric and electronic factors ruling the extent of electronic delocalisation in both **1** and **2** isomers.

Results and Discussion

Synthesis: The new complexes **2**-cod and **2**-nbd were synthesised by reaction of [{Rh(μ-Cl)(cod)}$_2$][11] and [{Rh(μ-Cl)(nbd)}$_2$],[12] respectively, with (2-ferrocenyl)indenyl potassium obtained by deprotonation of (2-ferrocenyl)indene[13] in THF at low temperature, similar to the procedure already reported for the isomeric complexes **1**-cod and **1**-nbd.[9a] Solvent removal under vacuum afforded the product as a red crystalline powder in 70–75% yield. Analogously to **1**-CO,[9a] the isomeric complex [$Rh(CO)_2\{\eta^5$-(2-ferrocenyl)indenyl}] (**2**-CO) was obtained in 50% yield by bubbling CO through a *n*-pentane/CH_2Cl_2 solution of **2**-cod. All the complexes exhibit spectroscopic data in accord with the proposed chemical structures (see Experimental Section). (2-Ferrocenyl)indene, **2**-cod and **2**-CO slowly crystallised from cold *n*-pentane/CH_2Cl_2 to give crystals suitable for single-crystal X-ray analysis. For the sake of simplicity, the atom labelling of the complexes in the NMR discussion follows IUPAC convention. In particular, the benzene ring protons and the a,a′ and b,b′ protons of the indenyl-bound Cp ring give rise to AA′BB′ systems and the H1–3 nuclei are uncoupled singlets, as expected on the basis of the molecular symmetry.

^{103}Rh NMR spectroscopy: The coupling of ^{103}Rh nucleus with the olefin protons of the ancillary ligands cod and nbd in complexes **2**-cod, **2**-nbd, **1**-cod and **1**-nbd, and with the H3 proton in complex **1**-CO, allowed the measurements of their ^{103}Rh chemical shifts $\delta(^{103}Rh)$, which are reported in Table 1 together with those of some reference compounds.

Table 1. ^{103}Rh-NMR chemical shifts.

Complex	$\delta(^{103}Rh)$[a]
1-cod	−381
2-cod	−345
Rh(cod)Cp	−785
Rh(cod)Ind	−487
Rh(cod)(η^3-cyclooctenyl)	−9
1-nbd	−398
2-nbd	−377
Rh(nbd)Cp	−786
Rh(nbd)Ind	−520
1-CO	−870
$Rh(CO)_2Cp$	−1321
$Rh(CO)_2Ind$	−1038

[a] In ppm; solvent CD_2Cl_2; T = 300 K.

All the ferrocenyl complexes display a downfield shift of the $\delta(^{103}Rh)$ with respect to Cp-RhL_2 and indenyl-RhL_2. For instance, the $\delta(^{103}Rh)$ of **2**-cod (−345 ppm) is 440 and 142 ppm less negative than those of cyclopentadienyl–Rh(cod) ([Rh(cod)Cp]) and indenyl–Rh(cod) ([Rh(cod)Ind]) complexes, respectively. Similar downfield shifts have been observed for all the title compounds except for **2**-CO, for which H,^{103}Rh coupling is not measurable with the adopted procedure. We have previously shown[14] that the rhodium

hapticity and the electron density at the metal strongly affect the $\delta(^{103}Rh)$ value. In the series Cp–,[15] indenyl–,[14] and cyclooctenyl–Rh(cod)[16] the shift of the $\delta(^{103}Rh)$ signal is attributed to the increase of importance of the η^3 hapticity. In addition, the electron-withdrawing substituents at the indenyl ligand are expected to shift the resonance downfield, while the electron-donating ones to induce an upfield shift.[17] The downfield shift of $\delta(^{103}Rh)$ values observed for the ferrocenyl derivatives here investigated is not in accord with the donating nature of the ferrocenyl group, suggesting that the effect of this substituent increases the allyl nature of the rhodium–indenyl bonding mode, being somewhat more pronounced when ferrocenyl is at the 2-position in **2**-cod and **2**-nbd complexes.

In the ^{13}C spectrum the C1, C2, C3, C3a and C7a nuclei as well as the ferrocenyl quaternary Cj, and the nbd and cod olefin carbon atoms couple with ^{103}Rh as already reported for other indenyl analogues.[14,18]

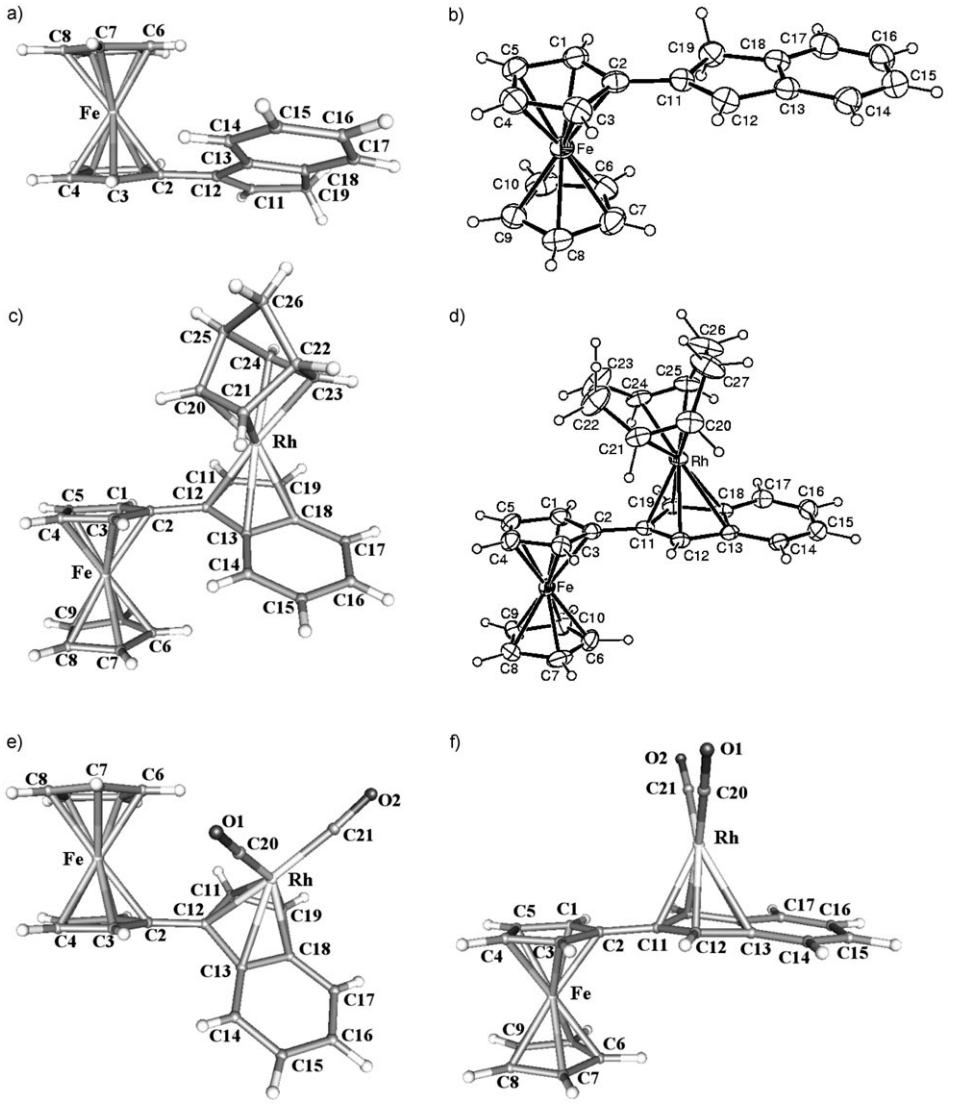

Figure 1. Molecular structures of a) (1-ferrocenyl)indene (X-ray),[9a] b) (2-ferrocenyl)indene (X-ray), c) **1**-nbd (X-ray),[9a] d) **2**-cod (X-ray), e) **1**-CO (X-ray)[9a] and f) **2**-CO (DFT optimised geometry). Hydrogen atoms are not labelled for clarity.

Molecular structures: The molecular structures of (2-ferrocenyl)indene and **2**-cod are shown in Figure 1 together with the atom numbering scheme. In Figure 1 the ball and stick structures of (1-ferrocenyl)indene, **1**-nbd, **1**-CO and **2**-CO are also depicted. In Table 2 the most relevant geometrical parameters are reported.

The rigid planarity of (2-ferrocenyl)indene is imposed by an operative π-electron resonance in the corresponding conjugated atom grouping and in part by the requirement to make the Cp ring (C6 to C10) bisect the angle H19-C19-H19′ such that the contact interactions between H1 and H19, H19′ are minimised. Besides this feature, all the geometrical parameters of (2-ferrocenyl)indene are quite in the norm and the Cp rings of the ferrocenyl group are in the staggered conformation. The molecular structure of **2**-cod can be compared with confidence with the analogous complex **1**-nbd (Figure 1), with the two olefins bound to rhodium with a similar steric encumbrance (the analogous **1**-cod complex could not be crystallised). Both the structures of **2**-cod and **1**-nbd assume a *transoid* configuration. The role of steric hindrance against a hypothetical *cisoid* configuration, in which the ferrocenyl group would face the cod group at prohibitive contact distances, is easily conjecturable. The most relevant structural features of **2**-cod are 1) the large bending of the cod group towards the vicinal Cp of the ferrocenyl substituent (the dihedral angle between the planes C20,C21,C24,C25 and C11,C12,C18,C19 or C1,C2,C3,C4,C5 in the range of 18–19°), 2) the large value of the slippage parameter[19] $\Delta = 0.217$ and 3) the hinge angle[19] HA = 8.5°. In addition they seem to be reinforced by possible intramolecular π–hydrogen-bond interactions between H21 and H24 with the π-system C1,C2,C3,C4,C5 at H···Cp distances in the range of 2.9–3.0 Å. The large deshielding of the $\delta(^{103}Rh)$ signals observed in the ^{103}Rh NMR spectrum suggests that the same structure is substantially maintained in solution.

Table 2. Selected interatomic distances [Å] and angles [°] of the experimental and computed structures **1**-nbd, **1**-CO, **2**-cod and **2**-CO and of the mono-oxidised computed species **1**-nbd$^+$, **1**-CO$^+$, **2**-cod$^+$ and **2**-CO$^+$. The atom numbering scheme of Figure 1 is used.

	1-nbd[a,b]		**1**-nbd$^+$		**1**-CO[a,b]		**1**-CO$^+$		**2**-cod[a]		**2**-cod$^+$		**2**-CO[a]		**2**-CO$^+$			(2-Fc)ind[a]
Fe–Q1[c]	1.661	*1.646*	1.696	–	1.656	*1.645*	1.710	–	1.663	*1.649(1)*	1.690	–	1.661	*1.588*	1.708	–	–	*1.648(1)*
Fe–Q2[c]	1.668	*1.648*	1.711	–	1.666	*1.653*	1.717	–	1.666	*1.650(1)*	1.705	–	1.668	*1.625*	1.715	–	–	*1.655(1)*
Rh–Q[c]	2.015	*1.924*	2.017	–	2.039	*1.941*	2.023	–	2.026	*1.938(1)*	2.012	–	2.033	*1.956*	2.022	–	–	–
Fe–Rh	5.399	*5.251*	5.409	–	4.517	*4.365*	4.455	–	5.346	*5.178(2)*	5.291	–	5.356	*5.251*	5.335	–	–	–
Δ[d]	0.162	*0.093*	0.157	–	0.216	*0.148*	0.225	–	0.237	*0.217*	0.258	–	0.243	*0.214*	0.264	–	–	–
HA[e]	7.7	*6.1*	6.4	–	10.3	*9.7*	10.6	–	11.5	*8.5*	12.2	–	12.9	*15.9*	13.1	–	–	–

[a] Crystallographic values are reported in italics; standard deviations are indicated when available. [b] Experimental data from reference [9a]. [c] Q1, Q2 and Q denote, respectively, the centroids of the Cp rings of the ferrocenyl moiety and the centroid of the Cp portion of the indenyl moiety. [d] Slippage parameter defined in reference [19]. [e] Hinge angle defined in reference [19].

The molecular structure of **2**-CO assumes a *transoid* configuration, which is opposite to the *cisoid* structure of **1**-CO (Figure 1). The molecular structure of **2**-CO could not be refined under $R=0.13$, due to the poor quality of the crystals; however, it is low enough for assigning univocally its *transoid* configuration. In **1**-CO, the larger rotational freedom about the bond joining the ferrocenyl and the indenyl groups allowed a suitable conformation to establish a π–hydrogen-bond interaction between one CO group and one Cp hydrogen atom without upsetting the coordination geometry of the $Rh(CO)_2$ group. On the contrary, a severe distortion of the coordination geometry would be imposed in **2**-CO in order to maintain the rigid planarity of the ligand and allow at the same time the formation of a π–hydrogen interaction. As a consequence, a *cisoid* configuration is inhibited. Suitable models show that for a *cisoid* orientation of the $Rh(CO)_2$ group very short C···C, Rh···C, Rh···H and C···H contact distances in the range of 2.4–2.8 Å would arise. Interestingly, this explanation is confirmed by the structure of the two trimetallic complexes *trans*- and *cis*-[$Cr(CO)_3$\{η^5-(2-ferrocenyl)indenyl\}$Rh(CO)_2$][20] in which the $Rh(CO)_2$ group is always *transoid* with respect to the ferrocenyl group.

In conclusion, the molecular structures of **2**-cod and **2**-CO are mainly ruled by electronic factors. In contrast, the dominant factors in **1**-nbd and **1**-CO are steric requirements and the formation, where possible, of intramolecular π-hydrogen bonds.[9a] In addition, by comparing the extent of planarity of the Cp–indene ligand of both (1-ferrocenyl) and (2-ferrocenyl)indene precursors, it is evident that the deprotonation followed by complexation with RhL_2 group has little influence on the torsion angle between the C11,C12,C13,C18,C19 and C1,C2,C3,C4,C5 planes.

Electrochemistry and optical data: As complex **2**-cod is central to this study, we will first present the electrochemical and optical spectroscopy results for **2**-cod and its oxidation products together with those of **2**-nbd analogue, and compare them with those of the other title compounds in which the structure of the organic bridging ligand and the nature of the ancillary ligands are ad hoc modified.

As oxidation by CV of **1**-cod, **1**-nbd, **1**-CO and **2**-CO evidenced partial decomposition at room temperature and potential scan rate below 1–2 $V s^{-1}$, the optical spectra were measured at −20 °C in order to stabilise the radical cations. For sake of comparison, also the optical spectra of **2**-cod$^+$, which is stable even at low potential scan rate and at room temperature, were recorded at −20 °C.

Electrochemistry of 2-cod and 2-nbd: The anodic behaviour of **2**-cod, obtained by CV in CH_2Cl_2/0.1 mol dm^{-3} NBu_4PF_6 in the range of potential scan rates $0.1<\nu<200$ $V s^{-1}$, displays two one-electron waves which are fully reversible in Nernstian and chemical senses (Figure 2b).

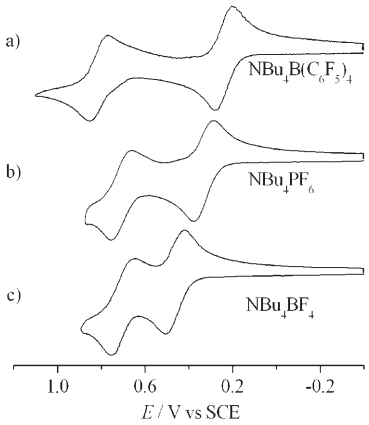

Figure 2. Cyclic voltammograms in CH_2Cl_2 at a gold disk electrode (diameter 0.5 mm), $T=20$ °C, scan rate $\nu=0.5$ $V s^{-1}$: a) **2**-cod with 0.1 mol dm^{-3} $NBu_4B(C_6F_5)_4$, b) **2**-cod with 0.1 mol dm^{-3} NBu_4PF_6 and c) **2**-cod with 0.1 mol dm^{-3} NBu_4BF_4.

Their separation $\Delta E_{1/2}$ is 370 mV. Similar results were found for **2**-nbd (Table 3) with $\Delta E_{1/2}=310$ mV. The magnitude of the $\Delta E_{1/2}$ has been frequently interpreted as a measure of the interaction between the metals. However, a cautionary warning on the use of the electrochemical data is required. In fact, voltammetric separations are influenced by other factors, in particular by the effect of the medium (solvent and supporting electrolyte), which can modify the electrostatic interaction in the dications.[21] In order to estimate how the supporting electrolyte regulates the $\Delta E_{1/2}$ values in the relatively low-polarity solvent CH_2Cl_2 we measured the anodic CV of **2**-cod with three tetrabutylammonium salts containing anions with different coordinating and ion-pair-

Table 3. Electrochemical data.[a]

bimetallic	E^1_p	E^2_p	$E^1_{1/2}$	$E^2_{1/2}$	$E^1_p-E^1_{p/2}$	$E^2_p-E^2_{p/2}$	$(i_{pc}/i_{pa})^1$	$(i_{pc}/i_{pa})^2$	$\Delta E_{1/2}$	K_c
1-cod[b]	0.21	0.63[e]	0.24	–	0.062	–	1[f]	–	–	–
1-cod[c]	0.43[g]	0.65[g]	0.40[g]	0.58[h]	0.067[g]	–	0.95[g]	0.65[g]	0.18	1.2×10^3
1-nbd[c]	0.40[f]	0.59[f]	0.39[f]	0.53[h]	0.060[f]	–	0.95[f]	0.75	0.14	2.6×10^2
1-CO[c]	0.57	0.96	0.54	–	0.069	–	0.96	–	–	–
2-cod[b]	0.27	0.86	0.25	0.83	0.055	0.069	1	1	0.58	9.4×10^9
2-cod[c]	0.36	0.74	0.33	0.70	0.063	0.068	0.96	0.95	0.37	2.3×10^6
2-cod[d]	0.50	0.74	0.46	0.70	0.063	0.072	0.95	0.95	0.24	1.3×10^4
2-nbd[c]	0.38	0.70	0.35	0.66	0.065	0.069	1	0.95	0.31	2.1×10^5
2-CO[b]	0.47	1.21	0.44	–	0.061	–	1	–	–	–
2-CO[c]	0.55[g]	0.81	0.51[g]	–	0.064[g]	–	0.95[f]	–	–	–

monometallic	E_p	$\Delta E_{1/2}$	$E_p-E_{p/2}$	i_{pc}/i_{pa}
ferrocene[b]	0.41	0.38	0.069	1
ferrocene[c]	0.51	0.48	0.063	1
ferrocene[d]	0.58	0.55	0.059	1
Rh(cod)Ind[b]	0.5[f]	0.47[f]	0.058[f]	0.5[f]
Rh(cod)Ind[c]	0.59[e]	0.56[e]	0.066[e]	0.58[e]
Rh(cod)Ind[d]	0.6[i]	0.57[i]	0.059[i]	0.92[i]
Rh(nbd)Ind[c]	0.59[g]	0.56[g]	0.059[g]	–
$Rh(CO)_2$Ind[c]	1.00[i]	0.97[i]	0.066[i]	–

[a] Solvent was CH_2Cl_2, scan rate 0.5 Vs^{-1} if not otherwise indicated; all potential are in volts relative to SCE; $T=20\,°C$. Supporting electrolyte 0.1 mol dm^{-3}. [b] $nBu_4NB(C_6F_5)_4$. [c] NBu_4NPF_6. [d] nBu_4NBF_4. [e] At a scan rate of 200 Vs^{-1}. [f] At a scan rate of 10 Vs^{-1}. [g] At a scan rate of 3 Vs^{-1}. [h] Estimated from $E^2_{pa}-E^2_{pc}$ middle potential. [i] At a scan rate of 100 Vs^{-1}. [j] Measured at 2600 Vs^{-1} in THF/nBu_4NBF_4.

ing ability in the order $BF_4^- \geq PF_6^- \gg B(C_6F_5)_4^-$, the last being a large weakly coordinating anion. Significant increase of $\Delta E_{1/2}$ is observed as the anion is changed from BF_4^- to PF_6^- to $B(C_6F_5)_4^-$, that is, 240, 370 and 580 mV respectively (Figure 2a–c and Table 3). This arises from the shift of $E^1_{1/2}$ to less positive potentials, similarly to the effect observed on the oxidation potential of ferrocene in the same media (Table 3), and from the shift of $E^2_{1/2}$ to more positive potential when the anion is $B(C_6F_5)_4^-$ due to diminishing ion-pairing of **2**-cod^{2+}.[21] This behaviour, which is similar to that already reported with the same electrolytes,[21] clearly indicates that a more realistic evaluation of $\Delta E_{1/2}$ is obtained with $nBu_4NB(C_6F_5)_4$ allowing the determination of ΔG_c and of the related comproportionation constant K_c (9.4×10^9) for the equilibrium given in Equation (1) (Table 3). The magnitude of K_c is indicative of high thermodynamic stability of **2**-cod$^+$ with respect to disproportionation.[3]

$$[Fe-Rh]+[Fe^+-Rh^+] \rightleftharpoons 2\,[Fe-Rh]^+ \qquad (1)$$

Finally, the electrochemical data allowed to calculate the energy difference ΔG_0 between the two states Fe^{III}-*spacer*-Rh^I and Fe^{II}-*spacer*-Rh^{II}. This difference (1210 cm^{-1}) can be obtained by the formula $[(E_{1/2}{}^{Rh(cod)Ind}-0.08)-E^1_{1/2}]$ in which $E_{1/2}{}^{Rh(cod)Ind}$ is the formal potential of the oxidation wave of monometallic Rh(cod)Ind at high scan rate when the redox process is fully reversible (Table 3), and 0.08 V represents the substituent effect of ferrocene.[22]

Near-IR spectra of 2-cod$^+$ and 2-nbd$^+$: As already mentioned, $\Delta E_{1/2}$ alone represents a poor quantitative parameter for evaluating the magnitude of the metal–metal interaction,[2n,22] and must be integrated by optical investigation in the near-IR region at which mixed-valence species typically absorb.

Both spectroelectrochemistry of **2**-cod in CH_2Cl_2/0.1 mol dm^{-3} nBu_4NPF_6 at applied potential from 0.2 to 0.4 V (scan rate $v=5$ mV s^{-1}) and chemical oxidation with one equivalent of acetylferrocinium tetrafluoroborate at $-20\,°C$ produced a blue solution of the monocation **2**-cod$^+$. The spectrum in the near-IR region (Figure 3, Table 4)

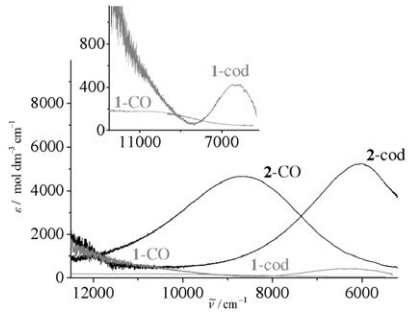

Figure 3. Near-IR spectroelectrochemistry at $-20\,°C$ and at applied potential from 0.2 to 0.4 V ($v=5$ mV s^{-1}) of 3.0 mol dm^{-3} **1**-cod, **2**-CO, **1**-CO in CH_2Cl_2/0.1 mol dm^{-3} nBu_4NPF_6 and of 3.0×10^{-3} mol dm^{-3} **2**-cod in CH_2Cl_2/0.1 mol dm^{-3} $nBu_4NB(C_6F_5)_4$.

showed the appearance of an intense and Gaussian-shaped absorption band at 6080 cm^{-1} ($\varepsilon_{max}=2620$ $mol^{-1}\,dm^3\,cm^{-1}$) typical of an intervalence transition (IT) of a mixed-valence species.[1–3]

Similarly, **2**-nbd$^+$ displayed an IT band at 6630 cm^{-1} ($\varepsilon_{max}=2480$ $mol^{-1}\,dm^3\,cm^{-1}$). IT transitions in dinuclear mixed-valence ions represent one of the most sensitive probe for electron-transfer processes. Their energy ($\tilde{\nu}_{max}$), intensity (ε_{max}), and half-bandwidth ($\Delta\tilde{\nu}_{1/2}$), are related to the electronic coupling (H_{ab}) and to the activation energy of the thermal electron transfer ($\Delta G^{\neq}$) through the two-state clas-

Table 4. NIR data.[a]

	$\tilde{\nu}_{max}$ [cm^{-1}]	ε_{max} [$mol\,dm^{-3}\,cm^{-1}$]	ΔG_0 [cm^{-1}]	$(\Delta\tilde{\nu}_{1/2})_{obsd}$ [cm^{-1}]	$(\Delta\tilde{\nu}_{1/2})_{calcd}$ [cm^{-1}]	H_{ab} [cm^{-1}]	$(H_{ab})_{DFT}$[b] [cm^{-1}]	α	$\Delta G^{\neq}$ [$kJ\,mol^{-1}$]
1-cod$^+$	5760	430	650	3210	3330	360[c]	–	0.063	15.7
1-nbd$^+$	6860	–	890	3570	3410	–	–	–	–
1-CO$^+$	10170	–	2820	3410	3790	–	–	–	–
2-cod$^+$[e]	6080	2620	1210	2250	3080	3040[d]	2413	0.5	–
2-nbd$^+$	6630	2480	1210	2240	3250	3315[d]	–	0.5	–
2-CO$^+$	8740	4680	3065	2740	3330	1420[c]	–	0.167	31.0

[a] Solvent was CH_2Cl_2/nBu$_4$NPF$_6$, $T=-20\,°C$. [b] H_{ab} [cm^{-1}] value calculated at B3LYP/LANL2DZ,6-31+G*. [c] Calculated by using Hush Equation (4) with $\lambda=\tilde{\nu}_{max}-\Delta G_0$. [d] Calculated by using Equation (3) with $\lambda=\tilde{\nu}_{max}$. [e] The data obtained in nBu$_4$NB(C$_6$F$_5$)$_4$ are $\tilde{\nu}_{max}=5860\,cm^{-1}$, $\varepsilon_{max}=5250\,mol\,cm^{-3}\,cm^{-1}$, $(\Delta\tilde{\nu}_{1/2})_{obs}=1990\,cm^{-1}$ $(\Delta\tilde{\nu}_{1/2})_{calcd}=3040\,cm^{-1}$, $H_{ab}=2940\,cm^{-1}$, $\alpha=0.5$.

sical Marcus–Hush theory.[3a] According to Robin and Day classification,[3c] three classes of mixed-valence systems can be distinguished on the basis of the magnitude of H_{ab}. The strength of electronic interaction between the oxidised and reduced sites ranges from essentially zero (Class I) to moderate (Class II), to very strong electronic coupling (Class III). Recently, Meyer and co-workers[3g] have defined borderline Class II/Class III systems, which exhibit both delocalised and localised behaviour. In the case of Class II regime $\Delta\nu_{1/2}$ can be calculated by using the Hush equations [Eqs. (2) and (3)], in which ΔG_0, is the energy difference between the two states Fe^{III}–spacer–Rh^{I} and Fe^{II}–spacer–Rh^{II} estimated from the $\Delta E_{1/2}$ values (Table 3 and 4), λ is the nuclear reorganisation energy, and $\tilde{\nu}_{max}$ the energy required for the optical electron transfer (E_{op}).

$$(\Delta\tilde{\nu}_{1/2})_{Hush}=[16\,RT\ln 2\lambda]^{1/2} \quad (2)$$

$$\lambda=\tilde{\nu}_{max}-\Delta G_0 \quad (3)$$

For the unsymmetrical mixed-valence ions **2**-cod$^+$ and **2**-nbd$^+$ (Table 4) the comparison between $(\Delta\tilde{\nu}_{1/2})_{obsd}$ and $(\Delta\tilde{\nu}_{1/2})_{Hush}$, which is usually diagnostic for the classification of a mixed-valence species, indicates that the experimental values (2250 and 2240 cm^{-1}) are much less than those predicted (3080 and 3250 cm^{-1}) for a Class II mixed-valence species, suggesting that **2**-cod$^+$ and **2**-nbd$^+$ are not valence trapped.

The classical Marcus–Hush analysis is known to fail when applied to systems with a significant donor–acceptor interaction, and thus it is not suitable to describe borderline Class-II/Class III compounds. Nevertheless it is traditionally employed and a disagreement between the calculated and the experimental values is ascribed to the presence of a rather strong interaction. More complex models should be used for borderline Class II/Class III or even Class III complexes, in which more than two electronic states are included[3j] or a detailed quantum chemical study is applied.[3k]

To assess further on the mixed-valence nature of **2**-cod$^+$ we studied the solvent effect on $\tilde{\nu}_{max}$ measuring the near-IR spectra in four solvents with noticeably different dielectric constants and donor numbers (DN), namely CH_2Cl_2 ($\tilde{\nu}_{max}=6080\,cm^{-1}$), CH_3NO_2 (6470 cm^{-1}), DMF (6700 cm^{-1}) and THF (6814 cm^{-1}). The largest blue shift of $\tilde{\nu}_{max}$(734 cm^{-1}) was observed by changing from CH_2Cl_2 to THF, which have almost identical dielectric parameters, in contrast to the expectation from Marcus–Hush and related non-equilibrium solvent polarisation theories. Moreover, THF possesses a much higher donicity (DN = 21) than CH_2Cl_2 (DN = 1), suggesting that specific solvent effects, or coupled high frequency vibrations in the solvent, could break down the dielectric continuum approximation.[3i] On the basis of 1) the low value of the half-bandwidth, 2) the large value of the equilibrium constant K_c, 3) the moderate solvent effect on the band energy and 4) the results of DFT calculations indicating electronic delocalisation in mixed-valence state (see DFT analysis), **2**-cod$^+$ can be assigned with good confidence to borderline Class II/Class III mixed-valence species, and the electronic coupling H_{ab} (3040 cm^{-1}) can be calculated by Equation (4), which is valid for this intermediate class of almost delocalised systems in which the thermal barrier $\Delta G^{\neq}$ is vanished and $\lambda=\tilde{\nu}_{max}$.

$$H_{ab}=\frac{\lambda}{2} \quad (4)$$

Electrochemistry of 2-CO: The voltammetric oxidation of **2**-CO in CH_2Cl_2/0.1 $mol\,dm^{-3}$ nBu$_4$NPF$_6$ at potential scan rate higher than 5 $V\,s^{-1}$ gave a fully chemically and electrochemically reversible one-electron response limited to the first wave at $E^1_{1/2}=0.51$ V vs. SCE (Table 3). A second oxidation wave is present at more positive potential in the range of E^2_p 0.8–1 V depending on the scan rate. However, it is not a diffusion-controlled process at all the potential scan rates investigated, with a typical stripping peak as cathodic counterpart at about 0.7 V (see Supporting Information). This indicates that the dication **2**-CO^{2+} produced at the level of the second wave precipitates on the gold electrode. The employment of nBu$_4$NB(C$_6$F$_5$)$_4$ increased the solubility of the dication and the corresponding redox process became diffusion controlled, but chemically irreversible, hampering an estimate of the formal potential of **2**-CO$^+$/**2**-CO^{2+}. The energy difference $\Delta G_0=3065\,cm^{-1}$ between the two ground states Fe^{III}-spacer-Rh^{I} and Fe^{II}-spacer-Rh^{II} was estimated (Table 4) from the expression $(E^{Rh(CO)_2Ind}_{1/2}-0.08)-E^1_{1/2}$, that is, the difference between the formal potential $E_{1/2}$ of Rh(CO)$_2$Ind at high scan rate when the redox process is Nernstian and $E^1_{1/2}$ of **2**-CO. Finally, the magnitude of K_c is indicative of rather high thermodynamic stability of **2**-CO$^+$ with respect to disproportionation.

IR and near-IR spectra of 2-CO$^+$: IR spectroelectrochemistry of **2**-CO in CH_2Cl_2/0.1 $mol\,dm^{-3}$ nBu$_4$NPF$_6$ at −20 °C and applied potential from 0.2 to 0.6 V vs. SCE (Figure 4a)

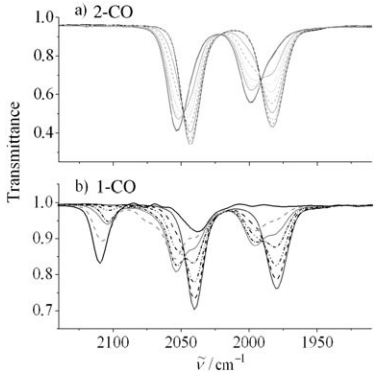

Figure 4. IR spectroelectrochemistry in CH_2Cl_2/0.1 mol dm^{-3} nBu$_4$NPF$_6$, at −20 °C, applied potential from 0.2 to 0.6 V, scan rate $v = 5$ mV s^{-1}, of a) **2**-CO and b) **1**-CO.

showed a shift of Rh(CO)$_2$ carbonyl stretching bands, A′ ($\Delta\tilde{\nu} = 10$ cm^{-1}) and A″ ($\Delta\tilde{\nu} = 15$ cm^{-1}), towards higher wavenumbers with respect to the initial spectrum of the neutral **2**-CO (2043, 1983 cm^{-1}), which completely disappeared to form the monocation **2**-CO$^+$. The small energy difference indicates that the positive charge is mainly localised on the iron centre.[22]

On the shorter timescale of the near-IR region, a very intense and Gaussian-shaped IT absorption band appeared at 8740 cm^{-1} ($\varepsilon_{max} = 4680$ mol^{-1} dm^3 cm^{-1}) for the mixed-valence species **2**-CO$^+$ (Figure 3, Table 4). The experimental half-bandwidth, $(\Delta\tilde{\nu}_{1/2})_{obsd} = 2740$ cm^{-1}, and that calculated by using the Hush equations [Eqs. (2) and (3)], $(\Delta\tilde{\nu}_{1/2})_{calcd} = 3330$ cm^{-1}, are quite similar as expected for a Class II mixed-valence species. Thus, the electronic coupling H_{ab} can be calculated by Hush Equation (5),[3a] in which d is unknown and represents the adiabatic electron transfer distance.

$$H_{ab} = \frac{0.0205(\varepsilon_{max}\tilde{\nu}_{max}\Delta\tilde{\nu}_{1/2})^{1/2}}{d} \quad (5)$$

This distance can be considerably shorter than the geometrical metal–metal separation when electronic coupling is significant. As a consequence, by using the iron–rhodium distance in **2**-CO$^+$ obtained by DFT calculations (5.335 Å), we estimate a lower limit of H_{ab} (1420 cm^{-1}). The delocalisation coefficient α (0.167), which quantifies the degree of valence delocalisation in the ground state (i.e., the fraction of valence electronic charge transferred from the donor to the acceptor metal centres) was calculated by using Equation (6). Provided that $H_{ab} < (\lambda + \Delta G_0)$ and $|\Delta G_0| < \lambda$,[3h] for an unsymmetrical Class II mixed-valence species the thermal barrier $\Delta G^{\neq}$ is given by Equation (7).

$$\alpha = \frac{H_{ab}}{\tilde{\nu}_{max}} \quad (6)$$

$$\Delta G^{\neq} = \frac{\lambda}{4} + \frac{\Delta G_0}{2} + \frac{\Delta G_0^2}{4(\lambda - 2H_{ab})} - H_{ab} + \frac{H_{ab}^2}{(\lambda + E_0)} \quad (7)$$

As the energy difference ΔG_0 between the two states Fe^{III}-spacer-Rh^{I} and Fe^{II}-spacer-Rh^{II} of **2**-CO$^+$ (3065 cm^{-1}) is significantly high, but definitely smaller than λ (see Table 4), and H_{ab} is much less than $(\lambda + \Delta G_0)$, Equation (7) is valid giving $\Delta G^{\neq} = 2590$ cm^{-1} (31.0 kJ mol^{-1}).

Electrochemistry of 1-cod, 1-CO and 1-nbd: The results of the voltammetric oxidation of **1**-cod, **1**-CO and **1**-nbd in CH_2Cl_2/0.1 mol dm^{-3} nBu$_4$NPF$_6$ are described in details in the Supporting Information. The main electrochemical data are reported in Table 3. An estimate of the comproportionation constant K_c for **1**-cod$^+$ and **1**-nbd$^+$ (1.2×10^3 and 2.6×10^2, respectively) indicates a lower thermodynamic stability to disproportionation of 1-ferrocenyl isomers with respect to the 2-ferrocenyl isomers. The energy differences ΔG_0 between the two ground states Fe^{III}-spacer-Rh^{I} and Fe^{II}-spacer-Rh^{II} could be determined and are reported in Table 4.

Near-IR spectra of 1-cod$^+$: Spectroelectrochemistry at −20 °C in CH_2Cl_2/0.1 mol dm^{-3} nBu$_4$NPF$_6$ on **1**-cod at an applied potential from 0.2 to 0.4 V in the near-IR region (Figure 3 Table 4) showed the appearance of a low intensity and Gaussian-shaped IT absorption band at 5760 cm^{-1} ($\varepsilon_{max} = 430$ mol^{-1} dm^3 cm^{-1}) of the mixed-valence **1**-cod$^+$. This band is characterised by lower intensity than that observed for **2**-cod$^+$. Metal–metal electron coupling was probed by using Marcus–Hush theory by comparing the experimental half-bandwidth with that calculated by using Equations (2) and (3). In this case $(\Delta\tilde{\nu}_{1/2})_{calcd}$ and $(\Delta\tilde{\nu}_{1/2})_{obsd}$ are quite similar as expected for Class II mixed-valence species. Thus, for **1**-cod$^+$ a lower limit of the electronic coupling H_{ab} (360 cm^{-1}) and the delocalisation coefficient α (0.063) can be calculated by Equations (5) and (6), in which d (5.409 Å) is the through space metal–metal distance obtained by DFT calculations for **1**-nbd$^+$ (see DFT analysis). As in the case of **2**-CO$^+$, Equation (7), which is valid for unsymmetrical Class II mixed-valence species, gave the thermal barrier $\Delta G^{\neq}$ of 1309 cm^{-1} (15.7 kJ mol^{-1}).

IR spectra of 1-CO and near-IR spectra of 1-CO$^+$ and 1-nbd$^+$: In a previous paper[9a] devoted to the study of the oxidation mechanism of **1**-CO the results evidenced the existence of a chemical interaction between the two metals in the carbonylated complex favoured by the relative proximity of the two metal groups in the *cisoid* conformation. The oxidation proceeds through a route in which the oxidised iron works as a sink of electrons supplied by rhodium with the consequence that the activation of this centre mediated by the ferrocenyl group occurs at a potential far lower than that required for direct oxidation of the metal. On the basis of the CV data and their digital simulation, and of the spectroscopic characterisation by NMR and IR spectroscopy of the final dication **1**-CO^{2+}, the proposed mechanism[9a] for the oxidation of **1**-CO (Scheme 2) foresaw an EECC mechanism (path A) constituted by two subsequent one-electron heterogeneous transfers (EE) followed by two homogeneous reactions (C). In addition, an ECE-C mechanism (path B),

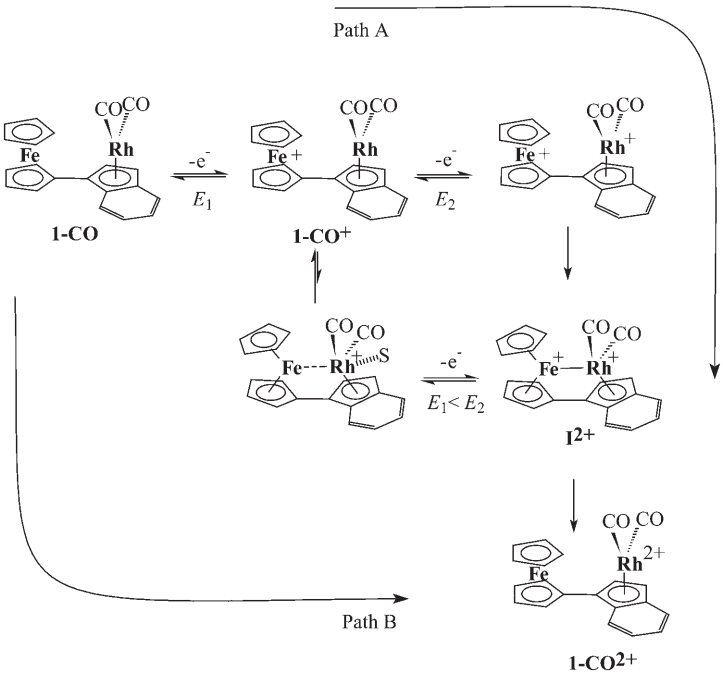

Scheme 2.

composed of two heterogeneous electron transfers (E) each followed by an homogeneous reaction (C), is present. Both paths produce the dication **1**-CO^{2+}. At long timescales and up to the potential of the first wave only the ECE-C mechanism (path B) occurs and the oxidation process tends to be bielectronic. IR spectroelectrochemistry in CH_2Cl_2/0.1 $mol^{-1}\,dm^{-3}$ nBu_4NPF_6 at −20 °C, applied potential from 0.2 to 0.6 V vs. SCE and scan rate $\nu = 5\,mV\,s^{-1}$ (Figure 4b), allowed us to study the process at the time scale of path B. In fact, at the onset of the first oxidation wave the initial IR spectrum of the neutral solution ($\tilde{\nu}$(C=O) 2040, 1980 cm^{-1}) began to decrease, and the CO stretching bands of **1**-CO^+ (2053, 1995 cm^{-1}) together with those of the dication intermediate $\mathbf{I}^{2+}$ (2103, 2028 cm^{-1}) concomitantly appeared. When the scan proceeded up to the potential of the second redox process, the bands of $\mathbf{I}^{2+}$ were replaced by two new ones at slightly higher wavenumber (2110, 2038 cm^{-1}) corresponding to the formation of the final dication **1**-CO^{2+}, the characteristics of which corresponds to those already reported.[9a] Upon cathodic scan reversal the **1**-CO was quantitatively recovered in the solution (≈95 %) and the initial IR spectrum was restored. These data support the path B of Scheme 2.

Near-IR spectroelectrochemistry of **1**-CO at −20 °C in CH_2Cl_2/0.1 $mol\,dm^{-3}$ nBu_4NPF_6 at applied potential from 0.2 to 0.6 V (Figure 3, Table 4) showed at the onset potential of the first oxidation wave the appearance of a low intensity IT band at 10170 cm^{-1} of the corresponding mixed-valence cation **1**-CO^+. Similarly to **1**-cod^+, the cation **1**-nbd^+ generated electrochemically in the LT-OTTLE cell gave an IT band at 6860 cm^{-1}. However, because of the instability of both **1**-CO^+ and **1**-nbd^+ ions, their concentrations and hence their maximum absorptivities ε_{max} could not be determined. As a consequence, the corresponding values of H_{ab} and ΔG^{+} could not be calculated. Conversely, the experimental half-bandwidths and those calculated by using Hush relationships [Eqs. (2) and (3)] were compared. In both the cases $(\Delta\tilde{\nu}_{1/2})_{calcd}$ and $(\Delta\tilde{\nu}_{1/2})_{obsd}$ are quite similar as expected for a Class II mixed-valence species.

UV/Vis spectra: The main absorption bands of the electronic spectra of **1**-CO, **1**-cod, **1**-nbd, **2**-CO and **2**-cod are given in the Supporting Information together with the computed excitation energies and the complete set of spectra. Intense absorptions between 200 and 300 nm are observed for the neutral species and are most likely assigned to ligand-based π–π* transitions and to Fe(dπ)–Cp(π*) charge transfer.[4] The absorption between 300 and 400 nm, in the visible spectrum of the neutral compounds, is more resolved for the 2-ferrocenyl isomers and is detected as a fused peak for the 1-ferrocenyl isomers. This band is responsible of the orange–yellow colour of the solution; the peaks of **2**-cod and **2**-CO, at 364 and 363 nm respectively, are slightly blue shifted with respect to the maxima of **1**-cod, **1**-nbd and **1**-CO, which occur at 346, 341 and 351 nm. No significant variation is observed on changing the ancillary ligands in the same isomer. It is worth noting that absorptions around 350 nm occur also in the monometallic indenyl RhL_2 complexes.

Upon oxidation, besides the IT band in the near-IR region (see near-IR results) a new band is observed in the visible spectra of **2**-cod^+ and **2**-CO^+ at 521 and 550 nm respectively. No new absorptions are found in the visible spectra of **1**-cod^+, **1**-nbd^+ and **1**-CO^+ (see Figure 5). This new band can probably be ascribed to a bridging-ligand-centred electronic transition. A detailed discussion of all these bands is presented in the DFT section.

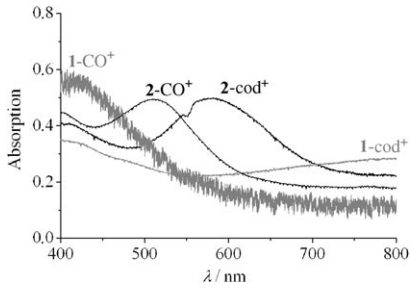

Figure 5. Visible spectra in CH_2Cl_2 of **2**-cod^+, **2**-CO^+, **1**-cod^+ and **1**-CO^+, obtained by oxidation of the neutral parent complexes with one equivalent of acetylferrocinium tetrafluoroborate at −20 °C.

DFT analysis: A computational study was undertaken in order to assess the role of the geometric and electronic factors tuning the extent of metal–metal interaction in the title compounds.

Full geometry optimisations have been carried out starting from the crystallographic structures of **1**-nbd,[23] **1**-CO, **2**-cod and **2**-CO (see section on Computational Methods). The most relevant interatomic distances and angles are re-

ported in Table 2; for comparison the experimental data are also indicated.

There is good agreement between the computed and the crystallographic structures. The strongest deviation is found for the position of rhodium with respect to the Cp moiety of the indenyl ring, that is, its distance from the centroid Q of the Cp ring and the slippage parameter Δ,[20] which are both overestimated. This discrepancy has already been observed in rhodium half-sandwich complexes at different levels of theory[24] and will not be further investigated in this context.

In the HOMOs of all four complexes, which are included in the Supporting Information, the lobes of the ferrocenyl moiety figure prominently.

The metal d contributions to the HOMO of **1**-nbd are 73.5% (Fe) and 2.0% (Rh). In contrast, in the HOMO of the carbonylated derivative **1**-CO, no significant contribution from rhodium d orbitals is present and the percentage contribution of Fe is 78.8%. In both complexes **1**-nbd and **1**-CO, the three highest occupied levels are essentially nonbonding levels of the ferrocenyl–indenyl fragment. Conversely, the inspection of the HOMOs of the isomers **2**-CO and **2**-cod reveals an appreciable contribution of rhodium d orbitals, that is, the percentage values of the metals are respectively 72.8% (Fe) and 1.1% (Rh) in the former and 63.3% (Fe) and 5.8% (Rh) in the latter compound. In addition, it is worth noting that the HOMO of **2**-cod is more delocalised over the molecular backbone then the HOMO of **1**-nbd, due to the participation of the HOMO-1 π level of the indenyl anion. The contribution of this indenyl π orbital is present in the HOMO-3 level of all four neutral compounds, but is present in the HOMO only in **2**-cod and in minor percentage in **2**-CO. The LUMOs of all four neutral species are mainly localised on the indenyl–RhL_2 fragment as a combination of Rh d orbitals with the HOMO π level of the indenyl anion, with some participation of iron for **2**-cod (21.3%) and **1**-nbd (17.6%).

The HOMO–LUMO gap is larger in **2**-cod than in **2**-CO, that is, 2.27 and 1.88 eV, respectively, and this is mainly due to the destabilisation of the LUMO of the former complex. The HOMO–LUMO gaps of **1**-nbd and of **1**-CO are 2.30 and 1.78 eV, respectively.

On the basis of the topology of the frontier orbitals of **1**-nbd, **1**-CO, **2**-cod and **2**-CO, the oxidation is expected to occur at the iron centre, as in Fe–Cr analogous compounds[5] and no significant structural variations are envisioned for the corresponding radical cations. Unrestricted full geometry optimisations were carried out starting from the optimised neutral geometries of **1**-nbd, **1**-CO, **2**-cod and **2**-CO to obtain the ions **1**-nbd$^+$, **1**-CO$^+$, **2**-cod$^+$ and **2**-CO$^+$. The good agreement between the crystallographic and the computed geometries of the neutral species allowed to predict with confidence the structures of these cations for which X-ray data are not available yet. The most relevant interatomic distances and angles are reported in Table 2. Upon oxidation the main structural changes involve the metal centres. The lengthening of the distances Fe–Q1 and Fe–Q2 (Q1 and Q2 denote the centroids of the Cp rings of the ferrocenyl moiety) by the average values 0.05 (**1**-CO) $\approx$ 0.05 (**2**-CO) $>$ 0.04 (**1**-nbd) $>$ 0.03 Å (**2**-cod), is accompanied by the shortening of the Rh–Q distances by 0.01 Å in all the cations, except **1**-nbd$^+$, indicating that the removal of one electron from iron affects also the rhodium environment. In addition, no significant variation of the extent of planarity of the bridges is predicted (Table 2).

According to the calculated adiabatic ionisation potentials, **2**-cod is more easily ionised with respect to **1**-CO and **2**-CO, due to the strongly electron-withdrawing character of the carbonyl ancillary ligands, and the values 5.88 (**2**-cod) $<$ 6.00 (**1**-nbd) $<$ 6.34 (**2**-CO) $<$ 6.53 eV (**1**-CO) reflect exactly the trend of the $E_{1/2}$ of the voltammetric first-wave (Table 3).

In the highest occupied spin orbitals of the four cations contributions are found from both the metals and from the HOMO-1 π level of the indenyl anion, which potentially provides the route for the electronic communication between rhodium and iron. To quantify the delocalisation of the unpaired electron in the mixed-valence species the spin density values were calculated (Table 5).

The spin density is localised on the metals, almost completely in **1**-CO$^+$ and **2**-CO$^+$. In addition, all the charged compounds are polarised; the spin density is prominently localised on iron, with an iron/rhodium ratio ranging from 7:1 in **1**-CO$^+$ to 2:1 in **2**-cod$^+$, the compound in which the most efficient metal–metal interaction is experimentally detected (Table 5).

Table 5. Mulliken spin densities calculated at ZORA/TZ2P all electron level of theory.

	Fe	Rh
1-nbd$^+$	0.6892	0.1333
1-CO$^+$	0.8042	0.1115
2-cod$^+$	0.5966	0.2682
2-CO$^+$	0.7669	0.1656

The assignment of the low-lying electronic transitions in the experimental spectra was performed by TD-DFT approach (see section on Computational Methods). The lowest fifteen vertical excitation energies were calculated for each neutral complex and the corresponding mixed-valence ion, covering approximately the 4000–30000 cm^{-1} region. The most intense computed transitions for **2**-cod and **2**-cod$^+$ are reported in Table 6; complete tables with the most relevant monoelectronic transitions for the other neutral and charged species are included in the Supporting Information.

The other calculated transitions exhibit much smaller oscillator strength and are not resolved in the experimental spectra. The employed level of theory was B3LYP/LANL2DZ,6-31+G*, due to the known performance of this hybrid functional in studying the excited states of complex systems.[2k,25] On the complexes **2**-cod$^{0/+1}$ TD-DFT calculations were carried out also at ZORA/TZ2P level, but a worse agreement of the energies with the experimental data was found. This is presumably to be ascribed also to a differ-

Table 6. Most important TD-DFT vertical excitation energies and oscillator strengths of **2**-cod, **1** $^{+}$and **2**-cod^{+}.

	Excited state	Orbital composition[a]	Coefficients	Excitation energy	Oscillator strength	Exptl value	Assignment
2-cod	7	H-6→L	0.126	358 nm (3.46 eV)	0.085	364 nm	MLCT
		H-6→L+2	0.198				
		H-5→L	−0.101				
		H-5→L+1	0.154				
		H-3→L	0.146				
		H-3→L+1	−0.219				
		H-1→L+3	0.129				
		H→L	−0.401				
		H→L+1	−0.262				
2-cod^{+}	2	(H-14)α→(L+1)α	−0.139	4826 cm^{-1} (0.60 eV)	0.084	6080 cm^{-1}	MMCT
		(H-13)α→Lα	0.163				
		(H-2)α→Lα	−0.114				
		Hα→Lα	−0.374				
		(H-13)β→Lβ	0.151				
		(H-8)β→Lβ	−0.395				
		(H-8)β→(L+1)β	0.109				
		(H-5)β→Lβ	0.124				
		Hβ→Lβ	1.020				
	13	(H-16)α→Lα	0.147	518 nm (2.39 eV)	0.146	572 nm	LMCT/MMCT
		(H-13)α→Lα	0.319				
		(H-12)α→Lα	0.216				
		(H-10)α→Lα	−0.134				
		Hα→Lα	0.583				
		(H-13)β→Lβ	0.139				
		(H-9)β→(L+1)β	−0.345				
		(H-8)β→(L+4)β	0.109				
		(H-5)β→Lβ	−0.216				
		Hβ→Lβ	0.107				
		Hβ→(L+1)β	0.490				

[a] Kohn–Sham HOMO and LUMO are indicated as H and L. Kohn–Sham HOMOα/β and LUMOα/β are indicated as Hα/β and Lα/β.

ent relative order of the frontier MOs; notably at ZORA/TZ2P level the MO of **2**-cod^{+} corresponding to (HOMO−1)β at B3LYP level is greatly stabilised and thus, while the values calculated for the parent neutral compounds are quite good, the TD-DFT energies computed for the open-shell cation are too high. Therefore in the following discussion only B3LYP results are used.

No absorptions are predicted in the near-IR spectral region for the neutral species, in agreement with the experiments. For **2**-cod and **1**-nbd the lowest computed energy absorption occurs in the visible range at 358 nm and 357 nm, respectively; these energy values compare nicely to the experimental peaks found, respectively at 364 nm for **2**-cod, 341 nm for **1**-nbd and 346 nm for **1**-cod. They are mainly HOMO-LUMO (Figure 6 a,b) and HOMO-LUMO+1 transitions. The analysis of the MOs involved in the various one-electron excitations allows to assign them to additive contributions of MLCT (Metal to Ligand Charge Transfer) transitions and d-d transitions within the ligand field formalism. Analogous absorptions of the same character, mainly due to HOMO-LUMO+1 transitions, are computed for the carbonylated complexes **1**-CO and **2**-CO at similar energy values, that is, 356 nm and 369 nm, respectively, in very good agreement with the experimental values 351 nm and 363 nm.

TD-DFT calculations on the mono-oxidised species predict allowed transitions in the near-IR spectral region. For **2**-cod^{+} the strongest absorption in the near-IR is calculated at 4826 cm^{-1} (0.60 eV), with oscillator strength 0.084, while the experimental band is centred at 6080 cm^{-1}. It is composed mainly of a mono-electronic transition HOMOβ–LUMOβ, which corresponds to the HOMO−1–HOMO transition in the neutral parent compound, and it has mainly MMCT (metal-to-metal charge transfer) character. The most important Kohn–Sham MOs of **2**-cod^{+} involved in this NIR absorption are shown in Figure 6c–f. It is worth noting that the calculated lowest excitation energy of **2**-cod^{+} at ZORA/TZ2P level is much higher than the experimental value, that is, 7807 cm^{-1} (f=0.054) versus the experimental value of 6080 cm^{-1}, but it has qualitatively the same composition of the excitation energy calculated at B3LYP/LANL2DZ,6-31+G* level of theory.

For **2**-CO^{+} the near-IR absorption is computed at 7254 cm^{-1} (0.90 eV) with oscillator strength 0.042; the experimental value is 8740 cm^{-1}. It is composed mainly of the mono-electronic transition HOMOβ–LUMOβ. Also in this case the band is assigned to a MMCT process.

Finally, the excitation energies computed in the near-IR region for **1**-nbd^{+} and **1**-CO^{+} are 6016 (0.75) and 8318 cm^{-1} (0.91 eV), respectively, with oscillator strengths 0.048 and 0.012, while the corresponding experimental values are 6860 and 10170 cm^{-1}. Also these bands can be assigned mainly to a MMCT process.

As mentioned in the UV/Vis section, the spectra of **2**-cod^{+} and **2**-CO^{+} are characterised also by an intense ab-

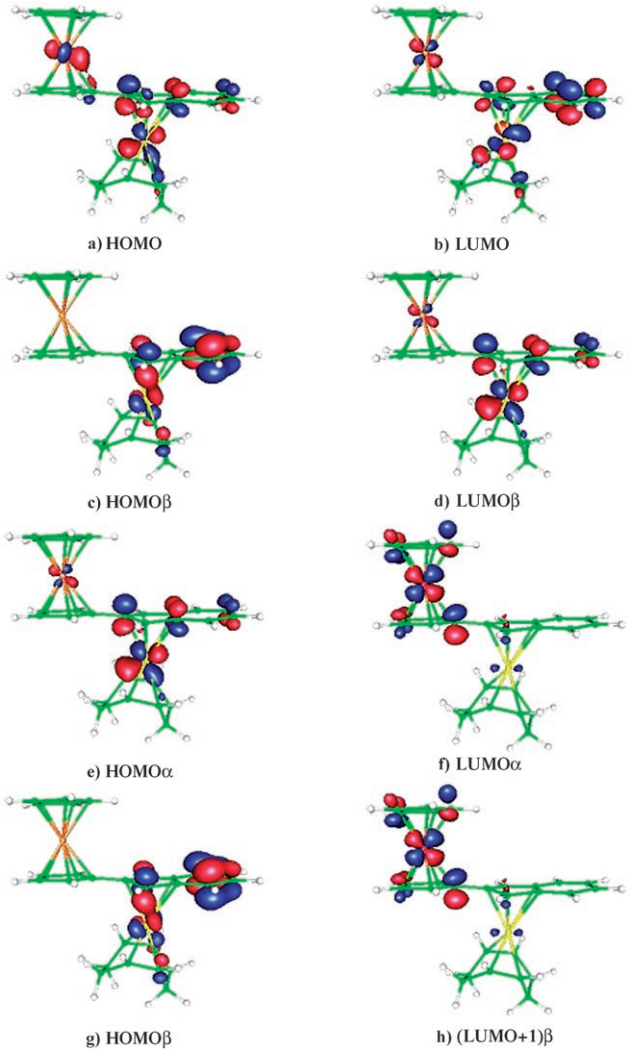

Figure 6. Selected couples of Kohn–Sham molecular orbitals involved in the TD-DFT calculated absorptions of the complexes **2**-cod$^{0/+1}$. Level of theory: B3LYP/LANL2DZ, 6-31+G*. Density: 0.04 $(e\,a_0^{-3})^{1/2}$.

sorption in the visible region at 572 and 502 nm. The computed values, 518 and 478 nm, are in good agreement with the experimental data. These absorptions are mainly composed by HOMOβ–LUMOβ and HOMOα–LUMOα transitions, similarly to what was found for the NIR bands (Figure 6c–h); in fact they can be assigned to additive MMCT and LMCT (ligand-to-metal charge transfer) processes. But notably, important contributions to these absorptions come also from low energy filled molecular orbitals to LUMO or LUMO+1 levels. These contributions are responsible for the blue shift of these bands.

Conclusion

The synthesis of a series of strictly correlated heterobimetallic isomers, that is, 1- and 2-Cp–indenyl-bridged iron–rhodium complexes with different ancillary ligands, has allowed a detailed study of the factors ruling the extent of electronic communication between the metal nuclei by a combination of voltammetric and spectroscopic techniques and by state of the art DFT calculations.

The crystallographic structures of the neutral compounds are characterised by a significant difference in the extent of symmetry and planarity of the Cp–indenyl bridging ligand: in the 1-ferrocenyl isomers the torsion angle about the σ C–C bond linking the Cp and the indenyl ring is about 30–40°, while it decreases to 5–10° in the 2-ferrocenyl isomers. These relevant geometric features, imposed by the interplay of both electronic and steric factors, are maintained upon oxidation, as predicted by DFT calculations, and strongly influence the iron–rhodium interaction. In fact, the importance of the almost planar 2-Cp–indenyl bridging ligand, which offers the possibility of a better electronic delocalisation than 1-Cp–indenyl, has been demonstrated on the basis of the experimental and computational results.

The $\Delta E_{1/2}$ separation between the two subsequent oxidation waves in the cyclic voltammetry has allowed us to determine the comproportionation constant K_c, which reflects the thermodynamic stability of the radical cations. It decreases of three orders of magnitude if 2-Cp–indenyl bridge in **2**-cod$^+$ ($K_c = 2.3\times10^6$) is replaced by 1-Cp–indenyl in **1**-cod$^+$ ($K_c = 1.2\times10^3$). The electrochemical $\Delta E_{1/2}$ is a poor quantitative parameter for determining the magnitude of the electronic coupling, or allocating Robin–Day mixed-valence classes, and it must be integrated by optical investigation on the radical cation intermediates.

For each of the examined mixed-valence cations a single near-IR band was detected. Its characteristics, the energy ($\tilde{\nu}_{max}$), intensity (ε_{max}), and half-bandwidth ($\Delta\tilde{\nu}_{1/2}$), allowed us to quantify the extent of the electronic coupling (H_{ab}) and the activation energy of the thermal electron transfer ($\Delta G^{\neq}$) through classical Marcus–Hush theory. The resulting values clearly indicate that the quasi-symmetric and almost planar 2-Cp–indenyl bridging ligand and the rhodium coordinated diolefin cod ($H_{ab} = 3040\ cm^{-1}$) and nbd ($H_{ab} = 3315\ cm^{-1}$) both contribute to ensure a more efficient electron transfer from rhodium to iron centres. In fact, according to Robin and Day classification **2**-cod$^+$ and **2**-nbd$^+$ are almost delocalised Class II/Class III mixed-valence species, while the electron coupling significantly decreases in **2**-CO$^+$ ($H_{ab} = 1420\ cm^{-1}$) and **1**-cod$^+$ ($H_{ab} = 360\ cm^{-1}$), which are Class II species.

It is worth noting that together with the near-IR band a second absorption in the visible spectrum has been experimentally detected only for the 2-Cp–indenyl-bridged mixed-valence species, that is, **2**-cod$^+$ and **2**-CO$^+$, which has been assigned to a LMCT/MMCT process by TD-DFT calculations. The presence of this second band, recently investigated both experimentally and theoretically by Lambert and co-workers in several organic mixed-valence systems,[26] can be associated with an alternative electron transfer pathway, in which the bridge serves as an intermediate electronic state allowing an incoherent electron hopping mechanism, the description of which requires at least a three-state model which goes beyond Marcus–Hush formalism.

In contrast to the efficiency of the 2-Cp–indenyl-bridging ligand in favouring the iron–rhodium interaction, the highly distorted arrangement of 1-Cp–indenyl bridge is found to lower the electronic communication in **1**-nbd$^+$, **1**-cod$^+$ and in **1**-CO$^+$. Finally, concerning the effect of the ancillary ligands on the extent of the electronic communication, replacement of cod and nbd with the strongly electron-withdrawing CO favours the trapping of the unpaired electron on the metal nuclei and thus lowers the electronic communication in **2**-CO$^+$ and **1**-CO$^+$.

Experimental Section

General procedures: All reactions and complex manipulations were performed in an oxygen and moisture-free atmosphere; *n*-pentane was deoxygenated before use. THF (Acros) was purified by distillation from Na/benzophenone under argon atmosphere and then oxygen freed with vacuum line techniques just before use. Ferrocene (Acros) was purified by crystallisation before use. (2-Ferrocenyl)indene and (3-ferrocenyl)indene (**3**) were synthesised according to the literature.[13] Crystals suitable for X-ray analysis were grown from solutions of the samples in *n*-pentane at −50 °C. Microanalyses were performed at the Dipartimento di Chimica Inorganica, Metallorganica ed Analitica, Università di Padova. IR spectra were recorded on a Bruker Equinox 55 FT-IR spectrometer. ^{1}H and ^{13}C NMR spectra were obtained in CD_2Cl_2 on a Bruker Avance DRX spectrometer operating at 400.13 and 100.61 MHz, respectively. The assignments of the proton resonances were performed by standard chemical shift correlation and NOESY experiments. The ^{13}C resonances were attributed through 2D-heterocorrelated COSY experiments (HMQC[27a] using gradient pulses with coherence selection step after T_1^2 and quadrature along F1 achieved using the TPPI method[27b–d] for the H-bonded carbon atoms, HMBC[27e,f] for the quaternary ones). All ^{103}Rh-NMR spectra (solvent CD_2Cl_2, $T = 300$ K) were recorded on Bruker Avance DRX spectrometer using a 5 mm inverse low frequency probe-head with a z-gradient coil (90-(^{1}H) = 7.50 μs, 90-(^{103}Rh) = 7 μs). The HMBC experiments were carried out using the sequence already reported.[27d] The spectral width for ^{1}H was 10 ppm. For ^{103}Rh the spectral width was initially 3000 ppm, and finally 500 ppm in order to improve resolution. The δ-(^{103}Rh) values are in ppm and were calculated by determining the absolute frequency of the cross peak and relating it to the arbitrary reference frequency ($\Xi = 3.16$ MHz at 100.00 MHz). The concentration of the samples was 6×10^{-2} mol dm^{-3}. CV experiments were performed in an air-tight three electrode cell connected to a vacuum/argon line. The reference electrode was a SCE (Tacussel ECS C10) separated from the solution by a bridge compartment filled with the same solvent/supporting electrolyte solution used in the cell. The counter electrode was a platinum spiral with an approximate 1 cm^2 apparent surface area. The working electrodes were disks obtained from cross section of gold wires of different diameters (0.5, 0.125 and 0.025 mm) sealed in glass. Between each CV scan the working electrodes were polished on alumina according to standard procedures and sonicated before use. An EG&G PAR-175 signal generator was used. The currents and potentials were recorded on a Lecroy 9310 L oscilloscope. The potentiostat was home-built with positive feedback loop for compensation of ohmic drop.[28] IR, near-IR, and visible spectroelectrochemistry experiments at variable temperatures were conducted with a cryostated (low-T) optically transparent thin-layer electrochemical (OTTLE) cell (IDEAS!UvA B.V., University of Amsterdam, The Netherlands)[29] equipped with CaF_2 windows. Pt working (80% transmittance), Pt auxiliary minigrid electrodes, and pseudo-reference Ag wire are melt-sealed in the insulating polyethylene spacer with optical path of 0.019 cm.

Synthesis of 2-cod: (2-Ferrocenyl)indene[13] (250 mg, 0.83 mmol) was metalated with excess KH in THF (50 mL) at −20 °C: the orange solution turned immediately to red. After 30 min the filtered solution was added dropwise to a solution of [{Rh(μ-Cl)(cod)}$_2$][11] (310 mg, 1.26 mmol) in THF (15 mL) and stirred for 45 min, while the temperature was raised slowly up to RT. The solvent was removed under vacuum and the residual (2-ferrocenyl)indene was extracted with cold pentane (5× 15 mL). The residue was extracted with CH_2Cl_2 and after filtration the solvent was removed. A reddish powder of the product, 248 mg (70%), was obtained upon removal of the solvent. Crystals suitable for single-crystal X-ray analysis were obtained by slow diffusion of *n*-pentane into a solution of **2**-cod in CH_2Cl_2 at −20 °C. M.p. 177–179 °C (decomp); elemental analysis calcd (%) for $C_{27}H_{27}FeRh$: C 63.55, H 5.33; found: C 63.33, H, 5.36; ^{1}H NMR (CD_2Cl_2, 400.13 MHz, internal reference Me_4Si): $\delta = 7.19$ (m, 2H; H4,H7), 7.02 (m, 2H; H5,H6), 5.35 (s, 2H; (H1,H3), 4.51 (m, 2H; Ha,Ha′), 4.23 (m, 2H; Hb,Hb′), 4.05 (s, 5H; C_5H_5 ring), 3.93 (m, 4H; cod olefin protons), 1.67 ppm (m, 8H; cod methylene protons); ^{13}C{^{1}H} NMR (CD_2Cl_2, 100.61 MHz, internal reference Me_4Si): $\delta =$ 122.55 (C5,C6), 119.16 (C4,C7), 114.04 ($^1J(^{103}Rh,^{13}C) = 2.0$ Hz, C3a, C7a), 111.33 ($^1J(^{103}Rh,^{13}C) = 5.4$ Hz, C2), 82.46 ($^2J(^{103}Rh,^{13}C) = 2.0$ Hz, Cj), 75.08 ($^1J(^{103}Rh,^{13}C) = 4.5$ Hz, C1,C3), 69.69 (C_5H_5), 68.40 (Cb,Cb′), 66.29 (Ca,Ca′), 68.94 ($^1J(^{103}Rh,^{13}C) = 14.8$ Hz, cod olefin carbon atoms), 31.56 ppm (cod methylene carbon atoms).

Synthesis of 2-nbd: (2-Ferrocenyl)indene[13] (250 mg, 0.83 mmol) was metalated with excess KH in THF (50 mL) at −20 °C: the orange solution turned immediately to red. After 30 min the filtered solution was added dropwise to a solution of [{Rh(μ-Cl)(cod)}$_2$][12] (290 mg, 1.25 mmol) in THF (15 mL) was added, and the solution was stirred for 60 min while the temperature was raised slowly up to RT. The solvent was removed under vacuum and the residual (2-ferrocenyl)indene was extracted with cold pentane (5×15 mL). The residue was extracted with CH_2Cl_2 and after filtration the solvent was removed. A reddish powder of the product (310 mg; 75%) was obtained upon removal of the solvent. Crystals suitable for single-crystal X-ray analysis were obtained by slow diffusion of *n*-pentane into a solution of **2**-nbd in CH_2Cl_2 at −20 °C. M.p. 121 °C; elemental analysis calcd (%) for $C_{26}H_{23}FeRh$: C 63.18, H 4.70; found: C 63.40, H, 4.72; ^{1}H NMR (CD_2Cl_2, 400.13 MHz, internal reference Me_4Si): $\delta = 7.25$ (m, 2H; H4,H7), 6.99 (m, 2H; H5,H6), 5.36 (s, 2H; (H1,H3), 4.50 (m, 2H; Ha,Ha′), 4.24 (m, 2H; Hb,Hb′), 4.05 (s, 5H; C_5H_5 ring), 3.27 (m, 4H; nbd olefin protons), 3.08 (m, 2H; nbd bridgehead protons), 0.83 ppm (m, 2H; nbd CH protons); ^{13}C{^{1}H} NMR (CD_2Cl_2, 100.61 MHz, internal reference Me_4Si): $\delta = 121.86$ (C5,C6), 119.23 (C4,C7), 110.53 ($^1J(^{103}Rh,^{13}C) = 2.4$ Hz, C3a, C7a), 82.88 ($^2J(^{103}Rh,^{13}C) =$ 2.0 Hz, Cj), 72.37 ($^1J(^{103}Rh,^{13}C) = 4.5$ Hz, C1,C3), 69.66 (C_5H_5), 68.25 (Cb,Cb′), 66.83 (Ca,Ca′), 58.35 (nbd CH_2 carbon atoms), 47.90 ($^1J(^{103}Rh,^{13}C) = 2.6$ Hz, nbd bridgehead carbon atoms), 38.98 ($^1J(^{103}Rh,^{13}C) = 10.6$ Hz, nbd olefin carbon atoms).

Synthesis of 2-CO: A solution of complex **2**-cod (100 mg, 0.2 mmol) in a 3:1 mixture of *n*-pentane/CH_2Cl_2 (10 mL) was bubbled with CO for 2 h at RT and the solution concentrated to about 5 mL. From the orange solution at −78 °C an orange powder precipitated. Then the supernatant liquid was removed and the product washed with cool *n*-pentane (2× 1 mL). The powder was dried under a stream of argon to afford 47 mg (50% yield) of **2**-CO. Crystals suitable for single-crystal X-ray analysis were obtained by slowly diffusion of *n*-pentane into a solution of **2**-CO in CH_2Cl_2 at −20 °C. M.p. 114–116 °C; elemental analysis calcd (%) for $C_{21}H_{15}FeO_2Rh$: C 55.06, H 3.30; found: C 54.87, H 3.34; IR (CH_2Cl_2): $\tilde{\nu} =$ 2040(s), 1980 cm^{-1} (s); ^{1}H NMR (CD_2Cl_2, 400.13 MHz, internal reference Me_4Si): $\delta = 7.26$ (m, 2H; H4,H7), 7.11 (m, 2H; H5,H6), δ 5.99 (s, 2H; H1,H3), 4.47 (m, 2H; Ha,Ha′), 4.27 (m, 2H; Hb,Hb′), 4.10 ppm (s, 5H; C_5H_5 ring); ^{13}C{^{1}H} NMR (CD_2Cl_2, 100.61 MHz, internal reference Me_4Si): $\delta = 189.71$ ($^1J(^{103}Rh,^{13}C) = 88$ Hz, CO), 124.93 (C5,C6), 118.60 (C4,C7), 117.94 ($^1J(^{103}Rh,^{13}C) = 2.0$ Hz, C3a,C7a), 73.23 ($^1J(^{103}Rh,^{13}C) =$ 5.8 Hz, C1,C3), 79.32 ($^2J(^{103}Rh,^{13}C) \approx 1$ Hz, Cj), 73.23 ($^1J(^{103}Rh,^{13}C) =$ 4.1 Hz, C1,C3), 69.96 (C_5H_5), 66.83 (Ca,Ca′), 69.14 ppm (Cb,Cb′).

Computational methods: Density functional theory (DFT) full geometry optimisations were carried out by using the Amsterdam density functional (ADF) program.[30] Electron correlation was treated within the local density approximation (LDA) in the Vosko–Wilk–Nusair parametrisation[31] and the nonlocal corrections of Becke[32] and Perdew[33] were added to the exchange and correlation energies. The applied numerical integration procedure was developed by te Velde et al.[34] and the Hessian

matrix update method was implemented by Broyden–Fletcher–Goldfarb–Shanno.[35] The basis set used for the atoms in the optimisation procedures are TZP (triple-ζ Slater-type orbital (STO) basis, extended with a single-z polarisation function) frozen core up to 2p for Fe, TZP frozen core up to 3d for Rh, TZP frozen core up to 1 s for C and O, TZP for H. Spin contamination in the open shell calculations was monitored: the expectation value was in all cases very close to the exact value 0.75.

To explore the importance of relativistic effects, a full geometry optimisation was carried out on complex **1**-CO using the ZORA (zeroth order regular approximation) formalism.[36] In this case the same functional above described and TZP all electron basis sets were employed for all the atoms. No significant improvement with respect to the non-relativistic results was observed. The geometry parameters are reported in the Supporting Information.

Single-point energy calculations on the optimised neutral and charged geometries were carried out at ZORA/TZ2P all electron level of theory, employing the same functional above described, for an accurate description of the electronic structure.

TD-DFT calculations were performed by employing the B3LYP hybrid functional and a standard LANL2DZ ECP basis[37] for rhodium and iron, and 6-31+G*[37] for the other atoms, O, C and H, (this level of theory is denoted in the text as B3LYP/LANL2DZ,6-31+G*), as implemented in the software Gaussian 03 B.05.[38] This methodological approach was adopted both for neutral and charged species, due to the known performance of hybrid functionals in TDDFT calculations. The assignment of the excitation energies to the experimental bands was performed on the basis of the energy values and oscillator strengths; the error falls within the typical range of similar large and open-shell compounds.[2k,39,40] For comparison, TD-DFT calculations were carried out on **2**-cod$^{0/+1}$ with the Response module implemented in ADF 2005.01 at ZORA/TZ2P all electron level of theory, employing the same functional above described for the geometry optimisations. When these results are compared to B3LYP results, a worse agreement is found with the experimental spectra (see text and Supporting Information), which is also in accord to what reported by other authors[25b] and may also be in part ascribed to differences in the relative order of the involved MOs.

Acknowledgements

This work was supported by the Ministero dell'Istruzione, dell'Università e della Ricerca (MIUR) within PRAT 2002, PRIN 2003, and Attrezzature Scientifiche 2003 research projects. CINECA (Consorzio Interuniversitario di Calcolo del Nord-Est, Casalecchio di Reno, Italia) is greatly acknowledged for the generous allocation of their computational facilities.

[1] a) R. J. Crutchley, *Angew. Chem.* **2005**, *117*, 6610–6612; *Angew. Chem. Int. Ed.* **2005**, *44*, 6452–6454; b) R. M. Williams, L. De Cola, F. Hartl, J.-J. Lagref, J.-M. Planeix, A. De Cian, M. W. Hosseini, *Coord. Chem. Rev.* **2005**, *230*, 253–261; c) A. Ceccon, S. Santi, L. Orian, A. Bisello, *Coord. Chem. Rev.* **2004**, *248*, 683–724; d) N. Robertson, C. A. McGowan, *Chem. Soc. Rev.* **2003**, *32*, 96–103; e) T. E. Bitterwolf, *Coord. Chem. Rev.* **2000**, *206*, 419–450; f) W. Kaim, A. Klein, M. Glöckle, *Acc. Chem. Res.* **2000**, *33*, 755–763; g) S. Barlow, D. O'Hare, *Chem. Rev.* **1997**, *97*, 637–670; h) M. D. Ward, *Acc. Chem. Res.* **1998**, *31*, 842–851; i) L. De Cola, P. Belser, *Coord. Chem. Rev.* **1998**, *177*, 301–346; j) F. Paul, C. Lapinte, *Coord. Chem. Rev.* **1998**, *178–180*, 431–509; k) P. Belser, S. Bernhard, C. Blum, A. Beyeler, L. De Cola, V. Balzani, *Coord. Chem. Rev.* **1999**, *190–192*, 155–169; l) J. Heck, S. Dabek, T. Meyer-Friedrichsen, H. Wong, *Coord. Chem. Rev.* **1999**, *190–192*, 1217–1254; m) D. Astruc, *Acc. Chem. Res.* **1997**, *30*, 383–391; W. E. Geiger, *J. Organomet. Chem. Libr.* **1990**, *22*, 142–191.

[2] a) K. Heinze , K. Hempel, M. Beckmann, *Eur. J. Inorg. Chem.* **2006**, *10*, 2040–2050; b) J. C. Salsman, S. Ronco, C. H. Londergan, C. P. Kubiak, *Inorg. Chem.* **2006**, *45*, 547–554; c) S. I. Ghazala, F. Paul, L. Toupet, T. Roisnel, P. Hapiot, C. Lapinte, *J. Am. Chem. Soc.* **2006**, *128*, 2463–2476; d) H. Sun, J. Steeb, A. E. Kaifer, *J. Am. Chem. Soc.* **2006**, *128*, 2820–2821; e) F. A. Cotton, C. A. Murillo, D. Villagrán, R. Yu, *J. Am. Chem. Soc.* **2006**, *128*, 3281–3290; f) S. C. Jones, S. Barlow, D. O'Hare, *Chem. Eur. J.* **2005**, *11*, 4473-4481; g) T.-Y. Dong, K. Chen, M.-C. Lin, L. Lee, *Organometallics* **2005**, *24*, 4198–4226; h) P. H. Dinolfo, S. J. Lee, V. Coropceanu, J.-L. Brédas, J. T. Hupp, *Inorg. Chem.* **2005**, *44*, 5789–5797; i) G. Laus, C. E. Strasser, M. Holzer, K. Wurst, G. Pürstinger, K.-H. Ongania, M. Rauch, G. Bonn, H. Schottenberger, *Organometallics* **2005**, *24*, 6085–6093; j) A. C. Benniston, A. Harriman P. Li, C. A. Sams, M. D. Ward, *J. Am. Chem. Soc.* **2004**, *126*, 13630–13631; k) F. A. Cotton, C. Y Liu, C. A. Murillo, D. Villagrán, X. Wong, *J. Am. Chem. Soc.* **2004**, *126*, 14822–14831; l) K. M.-C. Wong, S. C.-F. Lam, C.-C. Ko, N. Zhu, V. W.-W. Yam, S. Roué, C. Lapinte, S. Fathallah, K. Costuas, S. Kahlal, J.-F. Halet, *Inorg. Chem.* **2003**, *42*, 7086–7097; m) S. Welter, K. Brunner, J. W. Hofstraat, L. De Cola, *Nature* 2003, 421, 54–57; n) S. C. Jones, T. Hascall, S. Barlow, D. O'Hare, *J. Am. Chem. Soc.* **2002**, *124*, 11610–11611; o) S. Barlow, *Inorg. Chem.* **2001**, *40*, 7047–7053; p) C. G. Atwood, W. E. Geiger, *J. Am. Chem. Soc.* **2000**, *122*, 5477–5485.

[3] a) C. C. Allen, N. S. Hush, *Prog. Inorg. Chem.* **1967**, *8*, 357–391; b) N. S. Hush, *Prog. Inorg. Chem.* **1967**, *8*, 391–444; c) M. B. Robin, P. Day, A *dv. Inorg. Chem. Radiochem.* **1967**, *10*, 247; d) C. Creutz, *Prog. Inorg. Chem.* **1983**, *30*, 1–73; e) D. E. Richardson, H. Taube, *Coord. Chem. Rev.* **1984**, *60*, 107–129; f) R. J. Crutchley, *Adv. Inorg. Chem.*, **1994**, *41*, 273–325; g) P. Chen, T. J. Meyer, *Chem. Rev.* **1998**, *98*, 1439–1477; h) B. S. Brunschwig, N. Sutin, *Coord. Chem. Rev.* **1999**, *187*, 233–254; i) K. D. Demadis, C. M. Haertshorn, T. J. Meyer, *Chem. Rev.* **2001**, *101*, 2655–2685; j) D. M. D'Alessandro, F. R. Keene, *Chem. Soc. Rev.* **2006**, *35*, 424–440; k) B. S. Brunschwig, C. Creutz, N. Sutin, *Chem. Soc. Rev.* **2002**, *31*, 168–184; l) J. P. Launay, *Chem. Soc. Rev.* **2001**, *30*, 386–397; m) one of the referees was concerned by the use of the mixed-valence terminology to discuss a heterobimetallic ion such as **2**-cod$^+$, affirming that also the neutral **2**-cod could be considered mixed-valence following Launey's definition, since two metals in different oxidation states are present. We believe that Launey's definition may be extended to heteronuclear systems by interpreting that each metal exists in different oxidation states. Strictly speaking, a mixed-valence species exists in two valence isomers: in the case of **2**-cod$^+$ it exists as $[Fe^{III}\cdot Rh^{I}]^+$ and $[Fe^{II}\cdot Rh^{II}]^+$ between which a vectorial ET occurs and an IT band appears in the near-IR. In contrast, the neutral **2**-cod is not a mixed-valence compound, because it is described only as $[Fe^{II}\cdot Rh^{I}]$, the formation of $[Fe^{III}\cdot Rh^{0}]$ by internal ET being strongly disfavoured, and it is transparent in the NIR region. Examples of heterobimetallic species featuring unsaturated bridges in which two different metals are significantly coupled are quite rare. Among these, the species $[(Cp)Re(NO)\{PPh_3\text{-}C_4\text{-}(dppe)Fe(Cp)\}]^+$ reported by Lapinte and Gladysz was defined a mixed-valence radical ion: n) F. Paul, W. E. Meyer, L. Toupet, H. Jiao, J. A. Gladysz, C. Lapinte, *J. Am. Chem. Soc.* **2000**, *122*, 9405–9414.

[4] a) D. M. D'Alessandro, P. H. Dinolfo, J. T. Hupp, P. C. Junk, F. R. Keene, *Eur. J. Inorg. Chem.* **2006**, *4*, 772–783; b) D. M. D'Alessandro, F. R. Keene, *Chem. Eur. J.* **2005**, *11*, 3679–3688; c) D. M. D'Alessandro, F. R. Keene, *Aust. J. Chem.* **2005**, *58*, 767–777; d) D. M. D'Alessandro, P. C. Junk , F. R. Keene, *Supramol. Chem.* **2005**, 17, 529–542; e) J. Y. Chen, C.-H. Kao, S. J. Lin, C.-C. Tai, K. S. Kwan, *Inorg. Chem.* **2000**, *39*, 189–194; f) T.-Y Liu, J. Y. Chen, C.-C. Tai, K. S. Kwan, *Inorg. Chem.* **1999**, *38*, 674–679.

[5] S. Santi, A. Ceccon, A. Bisello, C. Durante, P. Ganis, L. Orian, F. Benetollo, L. Crociani, *Organometallics* **2005**, *24*, 4691–4694.

[6] a) A. Ceccon, A. Gambaro, S. Santi, A. Venzo, *J. Mol. Catal.* **1991**, *69*, L1–L6; b) L. Mantovani, A. Ceccon, A. Gambaro, S. Santi, P. Ganis, A. Venzo, *Organometallics* **1997**, *16*, 2682–2690.

[7] a) A. Borrini, P. Diversi, G. Ingrosso, A. Lucherini, G. Serra, *J. Mol. Catal.* **1985**, *30*, 181–189; b) P. Diversi, L. Ermini, G. Ingrosso, A. Lucherini, *J. Organomet. Chem.* **1993**, *447*, 291–298.
[8] a) F. Burgos, I. Chavez, J. M. Manriquez, M. Valderrama, E. Lago, E. Molins, F. Delpech, A. Castel, P. Riviere, *Organometallics* **2001**, *20*, 1287–1291.
[9] a) S. Santi, A. Ceccon, L. Crociani, F. Carli, A. Bisello, M. Tiso, A. Venzo, *Organometallics* **2002**, *21*, 2679–2686; b) A. Ceccon, A. Bisello, L. Crociani, A. Gambaro, P. Ganis, F. Manoli, S. Santi, A. Venzo, *J. Organomet. Chem.* **2000**, *600*, 94–111.
[10] R. G. Parr, W. Yang, *Density Functional Theory of Atoms and Molecules*, Oxford University Press, Oxford, **1989**.
[11] J. Chatt, M. L. Venanzi, *J. Chem. Soc.* **1957**, 4735–4751.
[12] E. W. Abel, M. A. Bennet, G. Wilkinson, *J. Chem. Soc.* **1959**, 3178–3182.
[13] H. Plenio, *Organometallics*, **1992**, *11*, 1856–1859.
[14] A. Ceccon, A. Gambaro, C. J. Elsevier, J. M. Ernsting, S. Santi, A. Venzo, *Inorg. Chim. Acta* **1993**, *204*, 15–26.
[15] R. Benn, A. Rufinska, *Angew. Chem.* **1986**, *98*, 851–871; *Angew. Chem. Int. Ed. Engl.* **1986**, *25*, 861–881.
[16] E. Maurer, S. Rieker, M. Schollbach, A. Schwenk, T. Egolf, W. von Philipsborn, *Helv. Chim. Acta* **1982**, *65*, 26–45.
[17] P. B. Graham, M. D. Rausch, K. Täschler, W. von Philipsborn, *Organometallics* **1991**, *10*, 3049–3052.
[18] a) A. Ceccon, A. Gambaro, S. Santi, G. Valle, A. Venzo, *J. Chem. Soc. Chem. Commun.* **1989**, 51–53; b) C. Bonifaci, A. Ceccon, A. Gambaro, P. Ganis, S. Santi, G. Valle, A. Venzo, *Organometallics* **1993**, *12*, 4211–4214.
[19] Δ is defined as $\Delta = 1/2[(\text{M-C1a} + \text{M-C3a}) - (\text{M-C1} + \text{M-C3})]$; HA is the dihedral angle between the planes C1,C2,C3 and C1,C3,C3a,C7a (referring to the numbering scheme of Scheme 1). T. B. Marder, J. C. Calabrese, D. C. Roe, T. H. Tulip, *Organometallics* **1987**, *6*, 2012–2014.
[20] C. Durante, S. Santi, A. Ceccon, A. Bisello, L. Orian, *XXII International Conference on Organometallic Chemistry*, Zagarosa, Spain, July 23–28, **2006**.
[21] a) F. Barriére, W. E. Geiger, *J. Am. Chem. Soc.* **2006**, *128*, 3980–3989; b) F. Barriére, N. Camire, W. E. Geiger, U. T. Mueller-Westerhoff, R. Sanders, *J. Am. Chem. Soc.* **2002**, *124*, 7262–7263; c) D. M. D'Alessandro, F. R. Keene, *Dalton Trans.* **2004**, 3950–3954.
[22] L. K. Yeung, J. E. Kim, Y. K. Chung, P. H. Rieger, D. A. Sweigart, *Organometallics* **1996**, *15*, 3891–3897.
[23] This complex was chosen for modelling purposes, since the crystallographic structure of **1**-cod is not available yet. Due to the similarity of the ancillary ligands cod and nbd, the results obtained in the present analysis for **1**-nbd$^{0/+}$ are still meaningful also when compared to the experimental data of **1**-cod$^{0/+}$, at least at qualitative levels, that is, when discussing trends of certain properties.
[24] a) L. Orian, A. Bisello, S. Santi, A. Ceccon, G. Saielli, *Chem. Eur. J.* **2004**, *10*, 4029–4040; b) L. Orian, P. Ganis, S. Santi, A. Ceccon, *J. Organomet. Chem.* **2005**, *690*, 482–492.
[25] a) G. J. Wilson, D. P. Arnold, *J. Phys. Chem. A* **2005**, *109*, 6104–6113; b) M. Doux, N. Mézailles, L. Ricard, P. Le Floch, P. D. Daz, M. J. Calhorda, T. Mahabiersing, F. Hartl, *Inorg. Chem.* **2005**, *44*, 9213–9224; c) M. Bühl, W. Thiel, *Inorg. Chem.* **2004**, *43*, 6377–6382.
[26] a) C. Lambert, S. Amthor, J. Schelter, *J. Phys. Chem. A* **2004**, *108*, 6474–6486; b) C. Lambert, C. Risko, V. Coropceanu, J. Schelter, S. Amthor, N. E. Gruhn, J. C. Durivage, J. L. Bredas, *J. Am. Chem. Soc.* **2005**, *127*, 8508–8516.
[27] a) A. Bax, S. Subramanian, *J. Magn. Reson.* **1986**, 67, 565–569; b) T. Parella *Magn. Reson. Chem.* **1998**, 36, 467–495; c) G. W. Vuister, J. Ruiz-Cabello, P. C. M. van Zijl, *J. Magn. Reson.* **1992**, 100, 282–302; d) W. Willker, D. Leibfritz, R. Kerrsebaum, W. Bermel, *Magn. Reson. Chem.* **1993**, 31, 287–292; e) A. Bax, M. F. Summers, *J. Am. Chem. Soc.* **1986**, 108, 2093–2094; f) M. F. Summers, L. G. Marzilli, A. Bax, *J. Am. Chem. Soc.* **1986**, 108, 4285–4294.
[28] C. Amatore, C. Lefrou, F. Pflüger, *J. Electroanal. Chem. Interfacial Electrochem.* **1989**, 270, 43–59.
[29] a) F. Hartl, H. Luyten, H. A. Nieuwenhuis, G. C. Schoemaker, *Appl. Spectrosc.* **1994**, *48*, 1522–1528; b) T. Mahabiersing, H. Luyten, R. C. Nieuwendam, F. Hartl, *Collect. Czech. Chem. Commun.* **2003**, *68*, 1687–1709.
[30] a) "Chemistry with ADF": G. te Velde, F. M. Bickelhaupt, S. J. A. van Gisbergen, C. Fonseca Guerra, E. J. Baerends, J. G. Snijders, T. Ziegler, *J. Comput. Chem.* **2001**, *22*, 931–967; b) C. Fonseca Guerra, J. G. Snijders, G. te Velde, E. J. Baerends, *Theor. Chem. Acc.* **1998**, *99*, 391–403; c) ADF 2005.01, SCM, Theoretical Chemistry, Vrije Universiteit, Amsterdam, The Netherlands, http://www.scm.com.
[31] S. D. Vosko, L. Wilk, M. Nusair, *Can. J. Phys.* **1980**, *58*, 1200–1211.
[32] a) A. D. Becke, *J. Chem. Phys.* **1986**, *84*, 4524–4529; b) A. D. Becke, *Phys. Rev. A* **1988**, *38*, 3098–3100.
[33] a) J. P. Perdew, *Phys. Rev. B* **1986**, *33*, 8822–8824; b) J. P. Perdew, *Phys. Rev. B* **1986**, *34*, 7406.
[34] G. te Velde, E. J. Baerends, *Int. J. Quantum Chem.* **1992**, *99*, 84–98.
[35] a) C. G. Broyden, *J. Inst. Math. Its Appl.* **1970**, *6*, 222–231; b) R. Fletcher, *Comput. J.* **1970**, *13*, 317–322; c) D. Goldfarb, *Math. Comput.* **1970**, *24*, 23–26; d) D. F. Shanno, *Math. Comput.* **1970**, *24*, 647–656.
[36] a) E. van Lenthe, A. E. Ehlers, E. J. Baerends, *J. Chem. Phys.* **1999**, *110*, 8943–8953; b) E. van Lenthe, E. J. Baerends, J. G. Snijders, *J. Chem. Phys.* **1993**, *99*, 4597–4610; c) E. van Lenthe, E. J. Baerends, J. G. Snijders, *J. Chem. Phys.* **1994**, *101*, 9783–9792; d) E. van Lenthe, J. G. Snijders, E. J. Baerends, *J. Chem. Phys.* **1996**, *105*, 6505–6516; e) E. van Lenthe, R. van Leeuwen, E. J. Baerends, J. G. Snijders, *Int. J. Quantum Chem.* **1996**, *57*, 281–293.
[37] Basis sets were obtained from the Extensible Computational Chemistry Environment Basis Set Database, Version 02/25/04, as developed and distributed by the Molecular Science Computing Facility, Environmental and Molecular Sciences Laboratory which is part of the Pacific Northwest Laboratory, P. O. Box 999, Richland, Washington 99352, USA, and funded by the U.S. Department of Energy. The Pacific Northwest Laboratory is a multi-program laboratory operated by Battelle Memorial Institute for the U.S. Department of Energy under contract DE-AC06–76RLO 1830. a) P. J. Hay, W. R. Wadt, *J. Chem. Phys.* **1985**, *82*, 270–283; b) P. J. Hay, W. R. Wadt, *J. Chem. Phys.* **1985**, *82*, 284–298; c) P. J. Hay, W. R. Wadt, *J. Chem. Phys.* **1985**, *82*, 299–310.
[38] Gaussian 03, Revision B.05, M. J. Frisch, G. W. Trucks, H. B. Schlegel, G. E. Scuseria, M. A. Robb, J. R. Cheeseman, J. A. Montgomery, Jr., T. Vreven, K. N. Kudin, J. C. Burant, J. M. Millam, S. S. Iyengar, J. Tomasi, V. Barone, B. Mennucci, M. Cossi, G. Scalmani, N. Rega, G. A. Petersson, H. Nakatsuji, M. Hada, M. Ehara, K. Toyota, R. Fukuda, J. Hasegawa, M. Ishida, T. Nakajima, Y. Honda, O. Kitao, H. Nakai, M. Klene, X. Li, J. E. Knox, H. P. Hratchian, J. B. Cross, V. Bakken, C. Adamo, J. Jaramillo, R. Gomperts, R. E. Stratmann, O. Yazyev, A. J. Austin, R. Cammi, C. Pomelli, J. W. Ochterski, P. Y. Ayala, K. Morokuma, G. A. Voth, P. Salvador, J. J. Dannenberg, V. G. Zakrzewski, S. Dapprich, A. D. Daniels, M. C. Strain, O. Farkas, D. K. Malick, A. D. Rabuck, K. Raghavachari, J. B. Foresman, J. V. Ortiz, Q. Cui, A. G. Baboul, S. Clifford, J. Cioslowski, B. B. Stefanov, G. Liu, A. Liashenko, P. Piskorz, I. Komaromi, R. L. Martin, D. J. Fox, T. Keith, M. A. Al-Laham, C. Y. Peng, A. Nanayakkara, M. Challacombe, P. M. W. Gill, B. Johnson, W. Chen, M. W. Wong, C. Gonzalez, J. A. Pople, Gaussian, Inc., Wallingford CT, **2004**.
[39] L. Medei, L. Orian, O. V. Semeikin, M. G. Peterleitner, N. A. Ustynyuk, S. Santi, C. Durante, A. Ricci, C. Lo Sterzo, *Eur. J. Inorg. Chem.* **2006**, 13, 2582–2597.
[40] F. Wang, T. Ziegler, *Mol. Phys.* **2004**, *102*, 2585–2595.

Received: May 24, 2006
Revised: September 5, 2006
Published online: December 15, 2006

